Case Studies in Thermal Engineering 61 (2024) 105070

Contents lists available at ScienceDirect

Case Studies in Thermal Engineering

journal homepage: www.elsevier.com/locate/csite

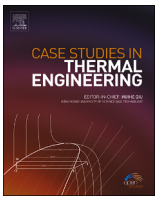

Investigation of temperature variations across the hot and cold sides of cascaded thermoelectric generator (CTEG) configurations in PV-CTEG hybrid systems

Abdelkader Rjafallah *, Daniel Tudor Cotfas, Petru Adrian Cotfas

Electrical Engineering and Computer Science Faculty, Transilvania University of Brasov, 500036, Brasov, Romania

ARTICLE INFO

Keywords:
Thermoelectric generator module
Cascaded thermoelectric generators modules
Uniform temperature distribution
Non-uniform temperature distribution
3D numerical simulation
COMSOL multiphysics

ABSTRACT

Cascaded thermoelectric generators (CTEGs) are increasingly used to enhance energy generation in photovoltaic (PV) cells under concentrated solar irradiance. However, research on temperature variation patterns on both sides of CTEGs, due to nonuniform irradiance and imperfect cooling, is limited. This paper explores a circular pattern, a central circular region surrounded by concentric rings, alongside a constant temperature. Experiments were conducted on PV-1,2,3-CTEG hybrid systems under irradiances of 230, 199, and 153 suns, using InGaP/InGaAs/Ge cells on Bi_2Te_3-CTEGs with water-cooled heat sinks. The current-voltage characteristics, short-circuit current (I_{sc}), open-circuit voltage (V_{oc}), and maximum power (P_{max}) were measured and compared with simulated results. The total P_{max} generated by the 1,2,3-CTEG configurations was 0.488 W, 0.718 W, and 0.461 W, respectively. Using COMSOL Multiphysics, the 1,2,3-CTEG configurations were simulated under three scenarios: (1) constant temperature on both sides, (2) a circular pattern on the top side, and (3) a circular pattern on both sides. Comparing the total P_{max} for the 1,2,3-CTEG configurations across scenarios (1)–(3) with experimental data, scenario (2) showed the closest alignment, with differences of 1 %, 5 %, and 10 %, respectively. This alignment was confirmed by the root mean square errors (RMSE), calculated as 0.178, 0.034, and 0.044 for scenarios (1)–(3), respectively.

Nomenclature

C_p	Specific heat capacity, J/(kg • K)
D	Electric flux density, C/m^2
E	Electric field intensity, V/m
I	Electric current, A
J	Electric density, A/m^2
P	Peltier coefficient, V
q	Heat flux, W/m^2
$\dot{q}$	Power density, W/m^3

(*continued on next page*)

* Corresponding author.
E-mail address: abdelkader.rjafallah@unitbv.ro (A. Rjafallah).

https://doi.org/10.1016/j.csite.2024.105070
Received 16 May 2024; Received in revised form 26 August 2024; Accepted 31 August 2024
Available online 5 September 2024

(*continued*)

Nomenclature	
Q	Heat, W
R	Electrical resistance, Ω
S	Seebeck coefficient, V/K
T	Absolute temperature, K
ΔT	Temperature difference, K
V	Electric potential, V
Greek symbols	
ε	Dielectric permittivity, F/m
k	Thermal conductivity, W/(m • K)
ρ	Density, kg/m^3
σ	Electrical conductivity, S/m
Subscripts	
c	Cold-side
h	Hot-side
in	Internal resistance
L	Electrical load
max	maximum
n	n-type leg
oc	Open-circuit
p	p-type leg
sc	Short-circuit
Abbreviations	
3D	Three Dimensional
CPV	Concentrating Photovoltaic
CTEG	Cascaded Thermoelectric Generator
EC	Evaporative Cooling
EL	Electronic Load
FEM	Finite Element Method
MT	Movable Table
PV	Photovoltaic
PVT	Photovoltaic Thermal
RMSE	Root Mean Square Error
STC	Solar Thermal Collector
STEG	Solar Thermoelectric Generator
TEC	Thermoelectric Cooler
TEG	Thermoelectric Generator
TEM	Thermoelectric Module

1. Introduction

Presently, energy consumption due to population growth and industrialization is experiencing an extraordinary increase. The primary energy source meeting this demand is fossil fuels, which are exhaustible resources and environmentally unfriendly. Consequently, the current prevailing trend is to transition towards renewable and green energy sources, which offer various advantages, such as being inexhaustible and environmentally friendly [1]. Therefore, they may provide a viable solution for the growing energy demand. Unfortunately, they are featured by being intermittent and relatively high expensive. The researchers and manufacturers strive to enhance the performance of present renewable energy solutions.

Solar energy stands out as a pivotal renewable energy source. The conversion of sunlight into electricity is achieved through the utilization of either flat-plate modules or concentrating solar panels. Flat-plate modules, a common solar technology, feature a flat, rectangular surface with photovoltaic (PV) cells mounted on it to absorb and convert sunlight into electrical energy. The term “flat-plate” denotes the module's simple design, distinguishing it from more intricate solar concentrating systems.

Concentrating solar panels are specifically designed to focus sunlight onto a small area for electricity generation. These systems utilize optical elements such as lenses or mirrors to concentrate sunlight onto high-efficiency solar cells. The distinctive attribute of concentrating solar panels lies in their ability to significantly increase electricity production efficiency compared to traditional flat-plate systems.

Flat-plate modules are known for their cost-effectiveness, offering approximately 23 % efficiency for single-junction cells. In contrast, CPV cells exhibit considerably higher efficiency, exceeding 47 % for six-junction III–V solar cells under 143 Suns concentration. The efficiency of these PV cells is influenced by various factors, with operating conditions playing a crucial role. Under real working conditions, PV cells can reach temperatures of 70–80 °C, leading to a reduction in maximum power by over 17 % [2].

Hence, reducing the operating temperature of PV cells is a crucial focus for research. Various solutions have been proposed in the literature, categorized as passive and active methods. Passive solutions include adding aluminum fins (heat sinks) to the back of PV panels [3–6], which can increase power yield by 5 % [7]. Other passive solutions involve modifying PV panel frame materials, frame geometry, and front surface geometry, as assessed through numerical testing [8].

Active cooling methods encompass replacing the heat sink with a solar thermal collector (STC), forming a photovoltaic thermal (PVT) system [9–13]. STCs not only lower the PV cell temperature but also generate thermal energy [14–16]. Another approach involves hybrid systems that integrate PV panels with thermoelectric modules (TEMs). TEMs can function as either thermoelectric coolers (TECs) in an active approach or as thermoelectric generators (TEGs) in a passive one [17].

TECs, utilizing the Peltier effect, generate a temperature difference between their sides when an electric current passes through them, with the cold side placed on the back of the PV panels. TEGs, based on the Seebeck effect, extract waste heat from the PV panels and convert it into electrical energy [18].

While TEGs offer advantages such as direct energy conversion, longevity, and scalability, their high module cost and relatively low efficiency have constrained widespread adoption [17,19]. The current industry focus is on reducing module costs through the discovery of more affordable and eco-friendly materials. Consequently, the integration of TEGs with PV panels has garnered increasing attention from both researchers and the industry.

This growing interest is evident in the numerous regular and review papers published over the last five years, addressing TEMs as individual components or their role in hybrid systems. These papers delve into various aspects, including the physical properties and manufacturing techniques of thermoelectric materials; enhancing their thermoelectric figure-of-merit [20]; the structure and geometry optimizations of TEMs [21]; the number and geometry of legs [22–30]; the use of TEMs for solar thermal energy generation [31]; improving PV performance through the use of TEMs, forming PV-TEG hybrid systems [32,33]; and the impact of temperature uniformity on either the hot or cold sides of TEMs [34–39].

Teffah et al. [40] experimentally and theoretically investigated the performance of a PV-TEC-TEG hybrid system under varying sun concentration ratios (300–1000). They reported that the PV's electric power generation increased with the increase of the sun concentration ratio, the TEC improved the PV's working conditions through effective cooling, and the TEG achieved a maximum efficiency of 5 %, thereby enhancing the overall efficiency of the hybrid system. Yin et al. [36] theoretically studied the performance of a solar thermoelectric generator (STEG) under six non-uniform illumination profiles using two-dimensional Gaussian distribution. They found that increasing the non-uniformity of solar illumination significantly raised the temperature in the central area of the hot side compared to its peripheral areas. Despite this impact on the temperature distribution, the maximum output power of the STEG decreases by only 1.4 %. Fallah Kohan et al. [41] theoretically investigated the performance of PV-TEG hybrid systems with varying numbers of TEG modules. Their findings indicate that the PV-TEG system produced a marginal increase of approximately 0.1 % in power output compared to a standalone PV cell under certain environmental conditions. Additionally, in the PV-1-TEG system, the temperature distribution was non-uniformly arranged in concentric circles, gradually decreasing from the center to the periphery in cases of high convection heat transfer from the TEG cold side. Lashin et al. [42] experimentally investigated the performance of CPV-TEG systems using two different PV cells with varying efficiencies and efficiency temperature coefficients, coupled to two different TEGs. They reported that enhancing the overall output power using TEGs can be effective if PV cells with a low efficiency temperature coefficient and high PV performance are selected. Additionally, TEGs should be chosen based on a high figure of merit. The efficiency of TEGs for various applications can be increased by maintaining the cold side at low temperatures. This can be achieved through several methods. One approach is to use a passive method with a heat sink with fins. Alternatively, active methods can be employed, such as using water [43] or nanofluids. Recently, nanofluids have been extensively studied, with discussions on their advantages and disadvantages [44–49]. Poddar et al. [50] numerically studied PV-1-CTEG, PV-2-CTEG, and PV-3-CTEG hybrid systems under solar concentration ratios ranging from 1 to 7. They reported that the temperature of the hybrid systems increased with the solar concentration ratio, reducing the efficiency of their respective PV cells. Additionally, at a concentration ratio of 7, the resultant efficiencies of PV-1-CTEG, PV-2-CTEG, and PV-3-CTEG were higher than that of the PV alone (15.71 %) by 2.15 %, 4.87 %, and 6.54 % respectively.

In contrast, there is a significant gap in research concerning the investigation of temperature variations on the top and bottom sides of the CTEGs in PV-CTEG hybrid systems. In our prior study [51], we examined temperature variations on the hot and cold sides of a TEG by investigating six circular and rectangular patterns of temperature variations. Unlike previous studies cited in our prior work, which mainly employed either a single central circle with varying diameters or identical squares with the same dimensions to simulate these nonuniform temperature variations on either the hot or cold sides of TEGs, our study explored other temperature variations.

The novelty and contributions of this paper are.

- Experimentally developing PV-CTEG hybrid systems with up to three CTEGs under concentrated light. Measuring the current-voltage characteristics of different components of the PV-CTEG hybrid systems, extracting electrical parameters such as short-circuit current, open-circuit voltage, maximum power, as well as measuring temperatures between the components.
- Theoretically, continuing our research on the temperature variation on the end sides of TEGs, exploring in the current study the temperature variation on the top and bottom sides of three CTEG configurations (1-CTEG, 2-CTEG, and 3-CTEG) using a circular pattern of temperature variation, as well as uniform temperature distribution. Using COMSOL Multiphysics, the three CTEG configurations were constructed and simulated under three distinct boundary condition scenarios: (1) constant temperature on both the top and bottom sides, (2) a circular pattern of temperature variation on the top side with constant temperature on the bottom side, and (3) a circular pattern of temperature variation on both the top and bottom sides. This approach provides novel insights into the temperature variation patterns on the top and bottom sides of the CTEG configurations, contributing to advancements in thermoelectric energy conversion.

- Performing a comparative analysis between the experimental and simulated results to achieve the best boundary condition scenario. The comparison was based on the short-circuit current, open-circuit voltage, and maximum power, and using the RMSE for the total maximum power.

Therefore, the rest of the article is structured as follows: Section 2 describes the materials and methodology used for simulating the three CTEG configurations for each boundary condition scenario and the experimental setup employed. This involves constructing numerical three-dimensional models using Comsol Multiphysics Software based on the Finite Element Method (FEM). The governing equations used in COMSOL Multiphysics are also presented. Section 3 outlines the results obtained from simulations and experiments. Simulation results provided by the three CTEG configurations under each scenario considered for each boundary condition are analyzed, discussed, and compared with the experimental results. Section 4 presents the conclusions drawn from this investigation and proposes some perspectives for future research.

2. Materials and methods

In this paper, the objective is to investigate a circular pattern of temperature variation on the top and bottom sides of three CTEG configurations, namely the 1-CTEG, 2-CTEG, and 3-CTEG configurations, using FEM-based Comsol Multiphysics software. The simulations of the entire PV-CTEG hybrid systems under high levels of solar irradiance, encompassing the solar radiation, PV cell, and CTEG configurations, will be the focus of a subsequent paper.

2.1. CTEG configurations

A three-dimensional model of a TEG, validated in a previous paper [51], was utilized to construct and simulate the three CTEG configurations (1-CTEG, 2-CTEG, and 3-CTEG). The TEG model underwent slight adjustments to align with the TEG employed in the three CTEG configurations. The TEG measures 40 mm × 40 mm × 3.4 mm and comprises 2 alumina ceramics plates, 255 copper interconnectors, and 127 pairs of p- and n-type legs made of Bismuth Telluride (Bi_2Te_3) semiconductor material. The legs are rectangular in shape and measure 1.4 mm × 1.4 mm × 1.8 mm (refer to Fig. 1a). Geometric dimensions of different components (alumina ceramics plates, copper interconnectors, and thermoelectric legs) of the TEG model are detailed in Table 1, along with the dimensions of the thermally conductive tape used between two CTEGs.

Fig. 1a–c illustrate the structural diagrams of the 1-CTEG, 2-CTEG, and 3-CTEG configurations, respectively, constructed in COMSOL Multiphysics software. The TEGs used to construct the 1-CTEG, 2-CTEG, and 3-CTEG configurations had the same dimensions and were placed one below the other, separated by a thermally conductive tape.

At the PV cell operating temperature, Bi_2Te_3 and its nano-composites are preferred thermoelectric materials [50]. Bi_2Te_3 is a standard thermoelectric material that exhibits the highest figure of merit within the temperature range below 250 °C. Therefore, Bi_2Te_3 was chosen as the thermoelectric material for the TEGs used in the experiments and simulations. This selection was also based on its extensive history of use in both non-commercial and commercial TEMs.

Additionally, the thermoelectric properties of Bi_2Te_3, such as the Seebeck coefficient, electrical conductivity, and thermal conductivity, are highly temperature-dependent, as illustrated in Fig. 2. Most previous research treats these thermoelectric properties as constants despite temperature variations, leading to inaccurate analyses. In the current study, the temperature dependency of Bi_2Te_3's thermoelectric properties is crucial, especially in simulating the three CTEG configurations under the second and third scenarios (i.e.,

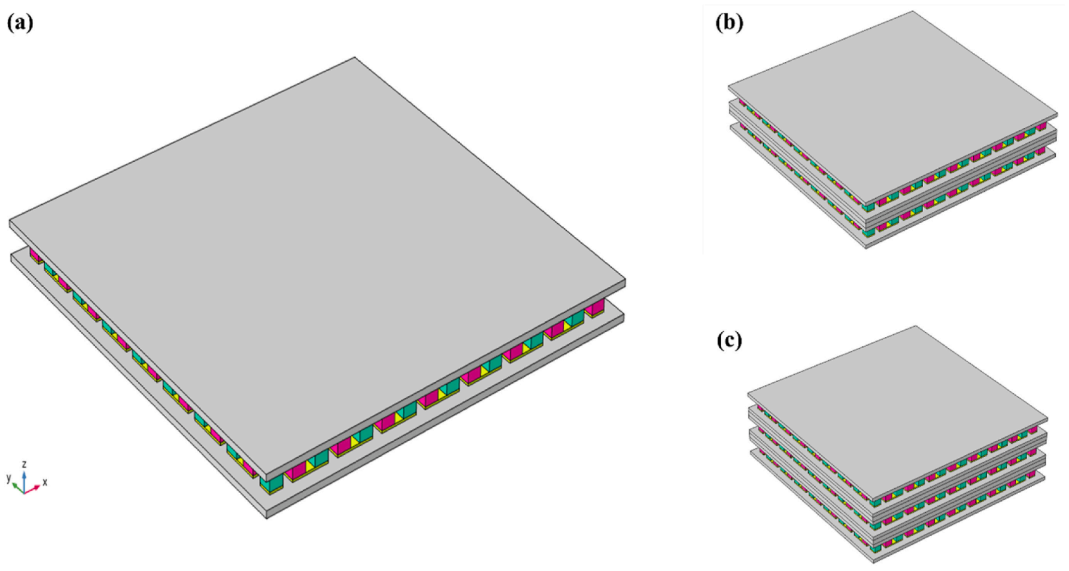

Fig. 1. The three CTEG configurations constructed in COMSOL Multiphysics software for this study: a) the 1-CTEG, composed of a single CTEG; b) the 2-CTEG, composed of two CTEGs separated by a thermally conductive tape; and c) the 3-CTEG, composed of three CTEGs separated by two thermally conductive tapes.

Table 1
Geometric dimensions of the components (alumina ceramics plates, copper interconnectors, and thermoelectric legs) of the TEG model along with the dimensions of the thermally conductive tape used to construct the 1-CTEG, 2-CTEG, and 3-CTEG configurations.

Name	Dimensions (mm)	Description
L_{TEG}	40	TEG length
W_{TEG}	40	TEG width
h_{TEG}	3.4	TEG height
$L_{Alumina}$	40	Alumina ceramics plates length
$W_{Alumina}$	40	Alumina ceramics plates width
$h_{Alumina}$	0.6	Alumina ceramics plates height
L_{Cu}	3.8	Copper interconnectors length
W_{Cu}	1.4	Copper interconnectors width
h_{Cu}	0.2	Copper interconnectors height
L_{Leg}	1.4	Thermoelectric legs length
W_{Leg}	1.4	Thermoelectric legs width
h_{Leg}	1.8	Thermoelectric legs height
d_{Pitch}	1	Distance between Thermoelectric legs
L_{Tape}	40	Thermally conductive tape length
W_{Tape}	40	Thermally conductive tape width
H_{Tape}	0.8	Thermally conductive tape height

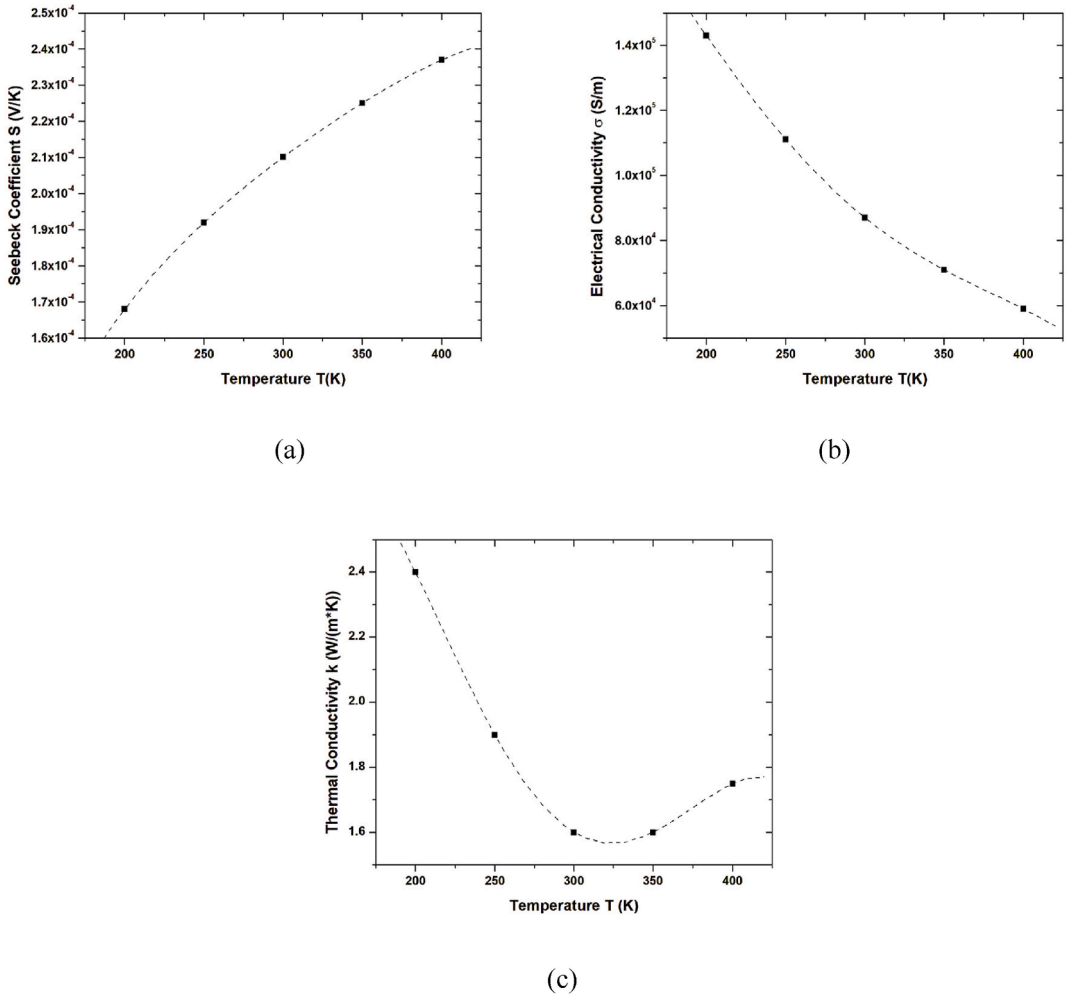

Fig. 2. Temperature dependency of a) Seebeck coefficient, b) electrical conductivity, and c) thermal conductivity for Bismuth Tellurides (Bi_2Te_3) semiconductor material, taken from the COMSOL Multiphysics materials library [52].

Nonuniform Temperature Across Top Side-Uniform Temperature Across Bottom Side and Nonuniform Temperatures Across Top and Bottom Sides). For the proposed circular pattern of non-uniform temperature distribution, which exhibits the highest temperature at the center and gradually decreases from the center to the periphery, the thermoelectric properties of Bi_2Te_3 must accurately reflect temperature variations.

Therefore, our numerical model considered the temperature dependency of Bi_2Te_3's thermoelectric properties for p- and n-type legs, as taken from the COMSOL Multiphysics materials library [52]. The material properties for alumina ceramics plates and copper interconnectors were sourced from the same library. The properties for thermally conductive tapes were obtained from the AG TermoPasty manufacturer [53]. All these properties are detailed in Table 2.

2.2. Assumptions and boundary conditions

The finite element simulations of the three CTEG configurations (1-CTEG, 2-CTEG, and 3-CTEG) under the three boundary conditions were carried out with the following assumptions and conditions.

- The CTEG configurations were analyzed using the following Physics Interfaces: Heat Transfer, Electric Currents, and Electrical Circuit.
- The CTEG configurations were studied in a steady-state.
- The CTEG configurations were considered isolated; they do not exchange anything with the surrounding air.
- The heat and electrical losses in the CTEG configurations were neglected.
- The alumina ceramics plates, copper interconnectors, and thermoelectric legs in the CTEG configurations were treated as three different homogenous substances with associated isotropic and constant thermophysical properties.
- The thermoelectric legs are made of Bi_2Te_3.
- The thermoelectric properties of the thermoelectric legs, such as the Seebeck coefficient, thermal conductivity, and electrical conductivity, were assumed to be temperature-dependent within the considered temperature ranges (refer to Fig. 2a–(c)).
- The thermal grease was considered between two CTEGs.
- The uniform and nonuniform temperature distributions were applied on the top and bottom sides of the CTEG configurations.

2.3. Theoretical aspects

In thermoelectricity analysis, the temperature distribution within the TEG module is governed by the heat flow general equation (1), while the continuity of electric charge is described by the electric charge continuity general equation (2), which are coupled by the thermoelectric constitutive equations (3) and (4). Additionally, a dielectric medium is characterized by the dielectric constitutive equation (5) [38].

$$\rho C_p \frac{\partial T}{\partial t} + \vec{\nabla} \cdot \vec{q} = \dot{q} \tag{1}$$

$$\vec{\nabla} \cdot \left(\vec{J} + \frac{\partial \vec{D}}{\partial t} \right) = 0 \tag{2}$$

$$\vec{q} = P\vec{J} - k\vec{\nabla}T \tag{3}$$

$$\vec{J} = \sigma \left(\vec{E} - S\vec{\nabla}T \right) \tag{4}$$

$$\vec{D} = \varepsilon \vec{E} \tag{5}$$

Where ρ represents the density of the material, which is the mass per unit volume (kg/m^3). It is a measure of how much mass is contained in a given volume. C_p represents the specific heat capacity, the amount of heat required to raise the temperature of a unit mass of the material by 1 K (J/(kg • K)). It is a measure of the thermal energy storage capacity of the material. T is the absolute temperature in Kelvin (K). It indicates the thermal state of a material. $\vec{q}$ is the heat flux vector, the rate of heat transfer per unit area (W/m^2). It indicates the flow of thermal energy through a surface. $\dot{q}$ is the power density, the volumetric heat generation rate (W/m^3). It represents the amount of heat generated per unit volume of the material. $\vec{J}$ is the electric current density vector, the electric current per unit area (A/m^2). It indicates the flow of electric charge through a surface. $\vec{D}$ is the electric flux density vector, the amount of electric flux pass-

Table 2
Material properties used in simulations for different components of the CTEG configurations [52,53].

Main components of CTEG configurations	Thermal conductivity κ (W/(m × K))	Electrical conductivity σ (S/m)	Specific heat capacity C_p (J/(kg × K))	Density ρ (kg/m^3)	Relative permittivity ε	Seebeck coefficient S (V/K)
Thermally conductive tapes	6	–	150	3000	–	0
Alumina ceramics plates	27	–	900	3900	–	0
Copper interconnectors	400	599.8×10^5	385	8940	1	6.5×10^{-6}
Bi_2Te_3 legs • p-type • n-type	κ(T) (Fig. 2c)	σ(T) (Fig. 2b)	154	7700	1	+S(T) (Fig. 2a) -S(T) (Fig. 2a)

ing through a unit area (C/m^2). It is related to the electric field and the material's permittivity. P (as defined in Eq. (6)) is the Peltier coefficient, a coefficient that relates the heat flux to the electric current (V). It is used in thermoelectric effects to describe the heat carried by an electric current. S is the Seebeck coefficient, a coefficient that relates the electric voltage to the temperature gradient (V/K). It is used in thermoelectric effects to describe the generation of electric voltage due to a temperature difference. k is the thermal conductivity, the ability of a material to conduct heat (W/(m • K)). It indicates how well heat is transferred through a material by conduction. σ is the electrical conductivity, the ability of a material to conduct electric current (S/m). It indicates how well electric charge is transported through a material. $\vec{E}$ (as defined in Eq. (7)) is the electric field intensity vector, the force per unit charge exerted on a charged particle (V/m). It represents the influence of electric charge on its surrounding space. V is the electric scalar potential. ε is the dielectric permittivity, the measure of a material's ability to store electrical energy in an electric field (F/m). It indicates how much electric flux is generated per unit electric field in the material.

$$P = ST \tag{6}$$

$$\vec{E} = -\vec{\nabla}V \tag{7}$$

Substituting equations (3)–(7) into equations (1) and (2) yields a system of coupled equations of thermoelectricity as follows [38,54]:

$$\rho C_p \frac{\partial T}{\partial t} - \vec{\nabla}\cdot\left(\sigma ST\vec{\nabla}V\right) - \vec{\nabla}\cdot\left(\sigma S^2 T\vec{\nabla}T\right) - \vec{\nabla}\cdot\left(k\vec{\nabla}T\right) - \sigma\vec{\nabla}V\cdot\vec{\nabla}V - \sigma S\vec{\nabla}T\cdot\vec{\nabla}V = 0 \tag{8}$$

$$\vec{\nabla}\cdot\left(\sigma\vec{\nabla}V\right) + \vec{\nabla}\cdot\left(\sigma S\vec{\nabla}T\right) + \vec{\nabla}\cdot\left(\varepsilon\vec{\nabla}\frac{\partial V}{\partial t}\right) = 0 \tag{9}$$

With,

$$\dot{q} = \vec{J}\cdot\vec{E} = \sigma\vec{\nabla}V\cdot\vec{\nabla}V + \sigma S\vec{\nabla}T\cdot\vec{\nabla}V \tag{10}$$

The thermoelectric analysis in the present model was conducted under steady-state conditions; therefore, the coupled equations of thermoelectricity can be rewritten as follows [51]:

$$\vec{\nabla}\cdot\left(\sigma ST\vec{\nabla}V\right) + \vec{\nabla}\cdot\left(\sigma S^2 T\vec{\nabla}T\right) + \vec{\nabla}\cdot\left(k\vec{\nabla}T\right) + \sigma\vec{\nabla}V\cdot\vec{\nabla}V + \sigma S\vec{\nabla}T\cdot\vec{\nabla}V = 0 \tag{11}$$

$$\vec{\nabla}\cdot\left(\sigma\vec{\nabla}V\right) + \vec{\nabla}\cdot\left(\sigma S\vec{\nabla}T\right) = 0 \tag{12}$$

The open circuit voltage V_{oc} generated by the TEG module when a temperature difference between the hot and cold sides is present is given by Ref. [28]:

$$V_{oc} = S\Delta T \tag{13}$$

Where $\Delta T = (T_h - T_c)$, T_h is the hot-side temperature, and T_c is the cold-side temperature.

The heat absorbed at the hot side Q_h and heat rejected from the cold side Q_c of the TEG module connected in series to electrical resistance R (see Fig. 3) are [41]:

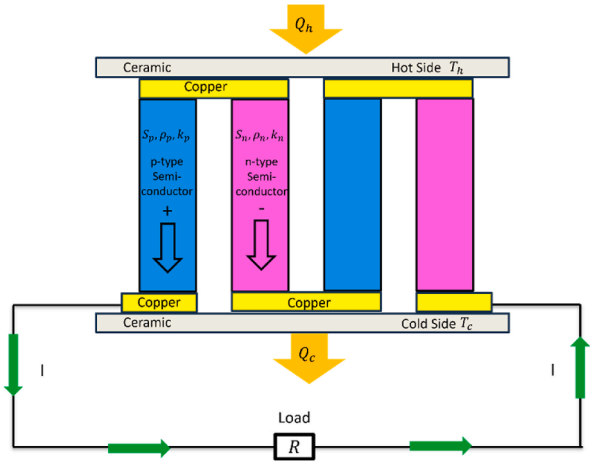

Fig. 3. Schematic diagram of a TEG connected in series with an electrical load [41].

$$Q_h = ST_hI - \frac{1}{2}R_{in}I^2 + K\Delta T \tag{14}$$

$$Q_c = ST_cI + \frac{1}{2}R_{in}I^2 + K\Delta T \tag{15}$$

Where S, R_{in}, and K are the total Seebeck coefficient (as defined in Eq. (16)), total internal resistance (as defined in Eq. (17)), and total thermal conductance (as defined in Eq. (18)) of pairs of p-type and n-type legs, respectively, and I is the electric current crossing the load resistance R (as defined in Eq. (21)) [40].

$$S = N\left(S_p - S_n\right) \tag{16}$$

$$R_{in} = N\left(\frac{\rho_p L_p}{A_p} + \frac{\rho_n L_n}{A_n}\right) \tag{17}$$

$$K = N\left(\frac{k_p A_p}{L_p} + \frac{k_n A_n}{L_n}\right) \tag{18}$$

Where N is the number of pairs of p-type and n-type legs in the TEG module, S_p is the Seebeck coefficient of p-type leg, S_n the Seebeck coefficient of n-type leg, ρ_p the electrical resistivity of p-type leg, ρ_n the electrical resistivity of n-type leg, k_p the thermal conductivity of p-type leg, k_n the thermal conductivity of n-type leg, A_p the cross-sectional area of p-type leg, A_n the cross-sectional area of n-type leg, L_p the length of p-type leg, and L_n is the length of n-type leg.

The total internal resistance of the TEG module was the sum of the electric resistances of all p-type and n-type leg pairs and copper electrodes. According to Table 2, the electric conductivity of the copper electrodes is 480 times greater than that of the p-type and n-type leg pairs. Therefore, the electric resistivity of the copper electrodes is much lower compared to that of the p-type and n-type leg pairs, and their electric resistance was omitted in the calculations for the sake of simplification.

By applying the first law of thermodynamics, the electric output power P provided by the TEG module to the load resistance R is given by Ref. [55]:

$$P = Q_h - Q_c = S\Delta TI - R_{in}I^2 \tag{19}$$

Moreover, the electric voltage V across the load resistance R, using Kirchhoff's Voltage Law, can be deduced as [55]:

$$V = V_{oc} - R_{in}I = S\Delta T - R_{in}I \tag{20}$$

Therefore, the electric current I crossing the load resistance R can be written as [26]:

$$I = \frac{V_{oc}}{R_{in} + R} = \frac{S\Delta T}{R_{in} + R} \tag{21}$$

Hence, the electric output power P provided to the load resistance R can be rewritten as [54]:

$$P = RI^2 = R\left(\frac{S\Delta T}{R_{in} + R}\right)^2 \tag{22}$$

The maximum output power P_{max} provided by the TEG module to the load resistance R is obtained when the external load resistance is nearly equal to the internal resistance of the TEG ($R = R_{in}$) as follows [32]:

$$P_{max} = \frac{1}{4}\frac{(S\Delta T)^2}{R} \tag{23}$$

2.4. Mesh sensitivity analysis

A finite element-based approach was employed to solve the governing equations of the model using the COMSOL Multiphysics 5.5 software. A mesh sensitivity analysis was conducted to explore the influence of mesh size on model outputs, utilizing three different mesh-element sizes: "Coarse," "Normal," and "Fine." For each mesh-element size, the three CTEG configurations were analyzed under uniform temperatures across the top and bottom sides (T_h = 71 °C – T_c = 19 °C for 1-CTEG, T_h = 109 °C – T_c = 19 °C for 2-CTEG, and T_h = 108 °C – T_c = 17 °C for 3-CTEG).

Free Tetrahedral meshing, a technique that generates tetrahedra elements without constraints on size or shape, was utilized in our finite element analysis-based computational simulations. Unlike structured meshes, which have a regular and structured arrangement of elements, free tetrahedral meshing offers greater flexibility in capturing complex geometries and can adapt to irregular shapes or regions with varying material properties. This flexibility makes free tetrahedral meshing well-suitable for modeling complex structures and phenomena in various engineering and scientific fields.

Table 3 presents the short-circuit currents (I_{sc}), open-circuit voltages (V_{oc}), and maximum powers (P_{max}) generated by the three CTEG configurations (1-CTEG, 2-CTEG, and 3-CTEG) for the three different mesh-element sizes. The study revealed that as the

Table 3
Mesh sensitivity analysis results for the three CTEG configurations.

Element size	Element number	Compon.	I_{sc} (A)	V_{oc} (V)	P_{max} (W)
1-CTEG configuration					
Coarse	92,519	TEG1	0.90811	2.3475	0.66174
Normal	145,723	TEG1	0.90784	2.3471	0.66143
Fine	365,461	TEG1	0.90708	2.3458	0.66054
2-CTEG configuration					
Coarse	195,384	TEG1	0.78790	2.0206	0.49576
		TEG2	0.66777	1.9996	0.42411
Normal	312,736	TEG1	0.78765	2.0201	0.49550
		TEG2	0.66755	1.9991	0.42389
Fine	782,478	TEG1	0.78695	2.0190	0.49479
		TEG2	0.66695	1.9979	0.42329
3-CTEG configuration					
Coarse	297,858	TEG1	0.54085	1.3381	0.22458
		TEG2	0.48905	1.3658	0.20985
		TEG3	0.43491	1.3286	0.18408
Normal	476,483	TEG1	0.54068	1.3378	0.22446
		TEG2	0.48890	1.3655	0.20975
		TEG3	0.43477	1.3283	0.18398
Fine	1,185,111	TEG1	0.54021	1.3371	0.22414
		TEG2	0.48847	1.3647	0.20945
		TEG3	0.43439	1.3275	0.18372

mesh-element size becomes finer, there is no significant change observed in I_{sc}, V_{oc}, and P_{max}. Therefore, the "Normal" mesh-element size was selected for the simulations, as it balances computation time and resource compatibility. For conciseness, Fig. 4 illustrates just the "Normal" size mesh generated using the Free Tetrahedral meshing technique for the three CTEG configurations.

2.5. Experimental setup

The experiments were conducted at the IMDEA ENERGY Institute in Mostoles-Madrid, Spain, using the KIRAN-42 high-flux solar simulator. The experimental setup is illustrated in Fig. 5. The setup (Fig. 5a) includes a Xenon lamp, a PV-CTEG hybrid system (Fig. 5b), a Gardon sensor, an alumina shield, an electronic characterization system, and a three-direction movable table (MT). The MT allows precise positioning of the target (either the PV-CTEG hybrid system or the Gardon sensor) relative to the lamp's focus.

The PV-CTEG hybrid system consists of a PV cell (1×1 cm^2) placed on a 5×5 cm^2 copper support and n-CTEGs (n = 1,2,3), situated on a water-cooled heat sink. The PV cell used in the experiments is an InGaP/InGaAs/Ge triple-junction cell with an efficiency of 39.6 % at an irradiance of 500 suns and a power temperature coefficient of −0.04 mW/°C [56]. The TEGs used in our experiments are commercial modules TEC1-12710, supplied by HB Corporation. The TEGs measure 40 mm × 40 mm × 3.4 mm and comprise 2 alumina ceramics plates, 255 copper interconnectors, and 127 pairs of p- and n-type legs made of Bi_2Te_3 semiconductor material. The

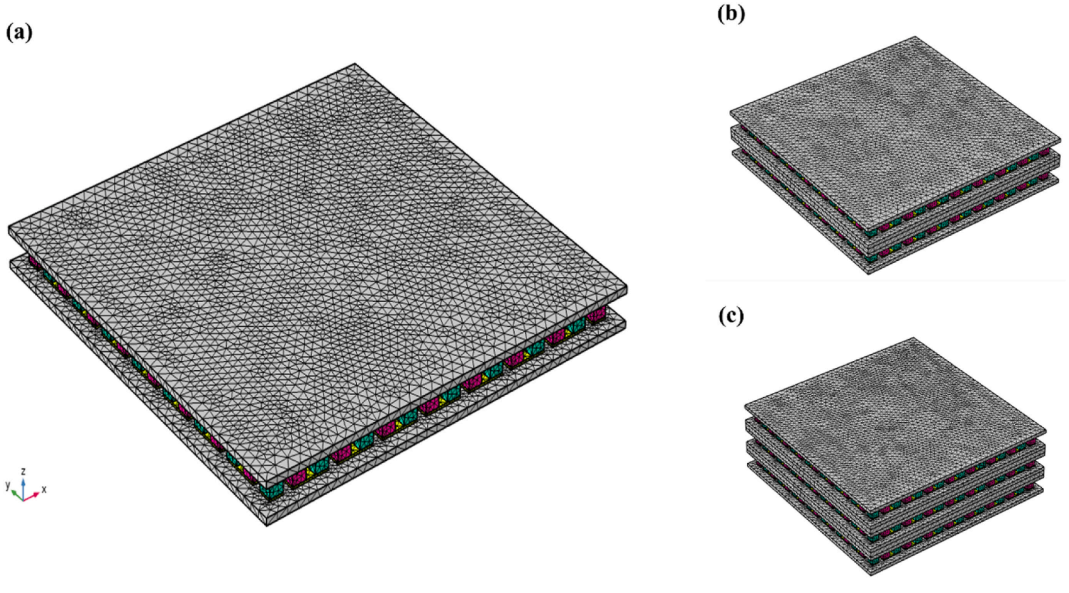

Fig. 4. "Normal" size-element mesh generated using the Free Tetrahedral meshing technique for a) the 1-CTEG, b) the 2-CTEG, and c) the 3-CTEG.

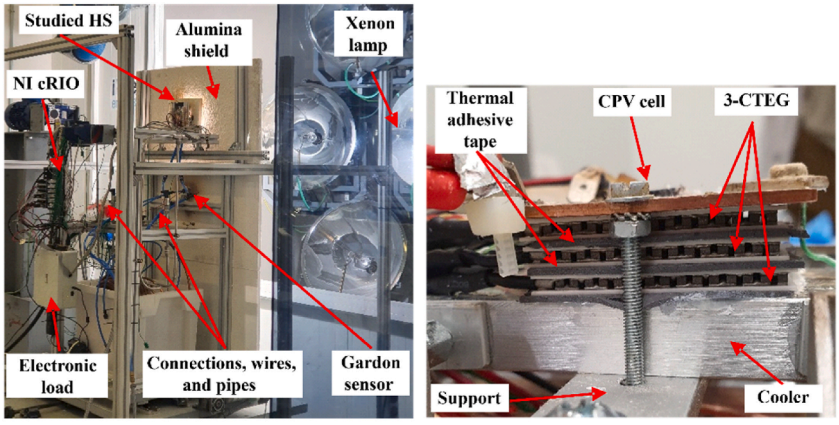

Fig. 5. Experimental setup: a) the entire test system; b) the PV-3-CTEG hybrid system.

legs are rectangular in shape, measuring 1.4 mm × 1.4 mm x 1.8 mm. Thermally conductive tape with a thickness of 1 mm (Fig. 5b) is used for connections between the CTEGs, facilitating thermal conductivity and temperature measurements between CTEGs via K-type thermocouples.

The electronic characterization system, built around the NI cRIO 9074 platform with appropriate I/O modules and a custom-designed electronic load, features four independent channels for measuring each component of the thermally connected PV-CTEG hybrid system. The system measures I-V characteristics, temperatures, and provides real-time short-circuit current (I_{sc}), open-circuit voltage (V_{oc}), and maximum power (P_{max}) data. Software applications for I-V characterization, temperature monitoring, and irradiance level measurements were developed using NI LabVIEW.

To establish the concentration ratio, a Gardon sensor was utilized, allowing irradiance levels to be set between 20 and 342 kW/m^2 in 20 kW/m^2 increments, with the MT used to adjust the target position relative to the lamp's focus. By determining the positions corresponding to these irradiance levels, the PV-CTEG hybrid system could be fixed at the desired irradiance level.

The experimental setup had some limitations. The use of thermocouples between components, especially between CTEGs, reduced thermal transfer. Eliminating thermocouples would allow the use of thinner thermal adhesive conductive tape (25 μm), enabling higher concentration ratios. This kind of hybrid system could be applied in PV panels coupled with CTEGs designed for concentrated light and potentially power intelligent sensor networks.

3. Results and discussion

3.1. Experimental results

The measurements were conducted on three PV-CTEG hybrid systems: PV-1-CTEG, PV-2-CTEG, and PV-3-CTEG. The irradiance measurements for the PV-1-CTEG, PV-2-CTEG, and PV-3-CTEG hybrid systems were 230 suns, 199 suns, and 153 suns, respectively. The I-V and P-V curves characterizing each component (PV cell and TEGs) of the three PV-CTEG hybrid systems under the measured irradiances were assessed separately. For conciseness, the measurement results, including the temperatures measured between different components (PV cell, TEGs, and Cooler) of each PV-CTEG hybrid system, as well as the I_{sc}, V_{oc}, and P_{max} provided by each TEG component, are presented in Tables 4–6.

By analyzing the experimental results, TEG1, the component of the 1-CTEG configuration, generated the highest P_{max} compared to any other TEG component in the 2-CTEG and 3-CTEG configurations. It was also noticed that the P_{max} generated by TEG components decreased from the 1-CTEG to the 3-CTEG configurations as the number of TEG components increased. If the P_{max} of the 1-CTEG configuration is considered as the reference P_{max}, the P_{max} generated by TEG1 and TEG2 were 32 % and 21 % lower, respectively, in the 2-CTEG configuration. For the 3-CTEG configuration, the P_{max} generated by TEG1, TEG2, and TEG3 were 73 %, 66 %, and 66 % lower, respectively. This decrease is due to the reduction in the temperature difference (ΔT) across each TEG component from the 1-

Table 4
Temperatures measured between different components (PV cell, TEG1, and Cooler) of the PV-1-CTEG hybrid system under a sun concentration ratio of 230, as well as I_{sc}, V_{oc}, and P_{max} generated by TEG1.

Hybrid System	PV Top	PV-TEG1	TEG1-Cooler	Compon.	I_{sc} (A)	V_{oc} (V)	P_{max} (W)
	T (°C)	T (°C)	T (°C)				
PV-1-CTEG	72.4	71.5	18.8	TEG1	1.189	1.648	0.488 (reference)

Table 5
Temperatures measured between different components (PV cell, TEG1, TEG2, and Cooler) of the PV-2-CTEG hybrid system under a sun concentration ratio of 199, as well as I_{sc}, V_{oc}, and P_{max} generated by TEG1 and TEG2.

Hybrid System	PV Top T (°C)	PV-TEG1 T (°C)	TEG1-TEG2 T (°C)	TEG2-Cooler T (°C)	Compon.	I_{sc} (A)	V_{oc} (V)	P_{max} (W)
PV-2-CTEG	106.3	109.4	66.7	18.8	TEG1	0.873	1.529	0.333 (−32 %)
					TEG2	1.082	1.428	0.385 (−21 %)

Table 6
Temperatures measured between different components (PV cell, TEG1, TEG2, TEG3, and Cooler) of the PV-3-CTEG hybrid system under a sun concentration ratio of 153, as well as I_{sc}, V_{oc}, and P_{max} generated by TEG1, TEG2, and TEG3.

Hybrid System	PV Top T (°C)	PV-TEG1 T (°C)	TEG1-TEG2 T (°C)	TEG2-TEG3 T (°C)	TEG3-Cooler T (°C)	Compon.	I_{sc} (A)	V_{oc} (V)	P_{max} (W)
PV-3-CTEG	115.5	107.7	78.6	46.9	16.9	TEG1	0.479	1.079	0.129 (−73 %)
						TEG2	0.675	0.988	0.166 (−66 %)
						TEG3	0.735	0.905	0.166 (−66 %)

CTEG to the 3-CTEG configurations. For the 1-CTEG, ΔT across TEG1 was 52.7 °C. For the 2-CTEG, ΔT across TEG1 and TEG2 were 42.7 °C and 47.9 °C, respectively. For the 3-CTEG, ΔT across TEG1, TEG2, and TEG3 were 29.1 °C, 31.7 °C, and 30 °C, respectively.

Additionally, when comparing the results generated by TEG1 and TEG2 in the 2-CTEG configuration, it was observed that TEG2, which is in contact with the heat sink, generated slightly more P_{max} than TEG1. Similarly, in the 3-CTEG configuration, TEG3, which is in contact with the heat sink, generated the same P_{max} as TEG2 and slightly more than TEG1. This is due to the heat sink effectively cooling the cold side of the last TEG in both the 2-CTEG and 3-CTEG configurations, while the cold sides of the upper TEGs are in contact with thermally conductive tape, where there are some thermal losses. Therefore, a slightly higher ΔT is observed across the last TEG than the upper TEGs, leading to slightly more P_{max} generated by the last TEG.

Moreover, when comparing the total ΔT across each CTEG configuration, it was observed that the ΔT across the 1-CTEG, 2-CTEG, and 3-CTEG configurations were 52.7 °C, 90.6 °C, and 90.8 °C, respectively. Therefore, the total ΔT increased with the number of CTEGs. This observation aligns with the findings reported in Ref. [50], which stated that the total ΔT can be increased by using thermal cascade, thereby enhancing the power output. When calculating the total P_{max} generated by each CTEG configuration, it was 0.488 W, 0.718 W, and 0.461 W for the 1-CTEG, 2-CTEG, and 3-CTEG configurations, respectively. It was noted that total P_{max} increased from the 1-CTEG to the 2-CTEG configurations but decreased from the 2-CTEG to the 3-CTEG configurations. This decrease is attributed to the PV-3-CTEG hybrid system receiving the lowest irradiance level (153 suns), while the PV-1-CTEG and PV-2-CTEG hybrid systems received 230 suns and 199 suns, respectively. Despite the irradiance level received by the PV-2-CTEG hybrid system being lower than that received by the PV-1-CTEG hybrid system, the total P_{max} increased due to the thermal cascade effect. The reduction in concentration ratio from 230 suns to 153 suns was necessary to not damage the PV.

3.2. Simulation results

Three CTEG configurations (1-CTEG, 2-CTEG, and 3-CTEG) were simulated under three boundary condition scenarios: (1) constant temperature on both the top and bottom sides, (2) a circular pattern of temperature variation on the top side with constant temperature on the bottom side, and (3) a circular pattern of temperature variation on both the top and bottom sides. The temperature data provided in Tables 4–6 were considered in simulations of these CTEG configurations under boundary condition scenarios (1)–(3), focusing on temperatures recorded on the top and bottom sides of each CTEG configuration. The I-V and P-V curves characterizing each TEG component in each CTEG configuration were extracted from the numerical model for all three boundary condition scenarios. For conciseness, these I-V and P-V curves were only presented for boundary condition scenario (1). The I_{sc}, V_{oc}, and P_{max} values were then extracted from the I-V and P-V curves and compared with the corresponding experimental results. The simulation was conducted on a computer equipped with an Intel Core i9 processor running at 3.6 GHz.

3.2.1. Scenario (1): constant temperature on both the top and bottom sides

- 1-CTEG *Configuration*

The performance of the 1-CTEG configuration under boundary condition scenario (1) was explored. According to Table 4, the temperatures measured on the top and bottom sides of the 1-CTEG configuration were 71.5 °C and 18.8 °C, respectively. These values were used as inputs for the numerical model designed to simulate the 1-CTEG configuration under boundary condition scenario (1), where constant temperatures of 71 °C (≈71.5 °C) and 19 °C (≈18.8 °C) were applied to the top and bottom sides, respectively.

Fig. 6 illustrates the resulting temperature distribution across the 1-CTEG configuration under these specified conditions. Fig. 7 depicts the temperature variation across the TEG1 component of the 1-CTEG configuration. The temperature varies linearly across the p-type (or n-type) leg of TEG1 due to its high thermal resistance, while it remains almost constant across the alumina ceramics plates and copper interconnectors due to their high thermal conductivities.

Fig. 8 illustrates the I-V and P-V curves of the TEG1 component of the 1-CTEG configuration. Table 7 presents the I_{sc}, V_{oc}, and P_{max} values extracted from these curves.

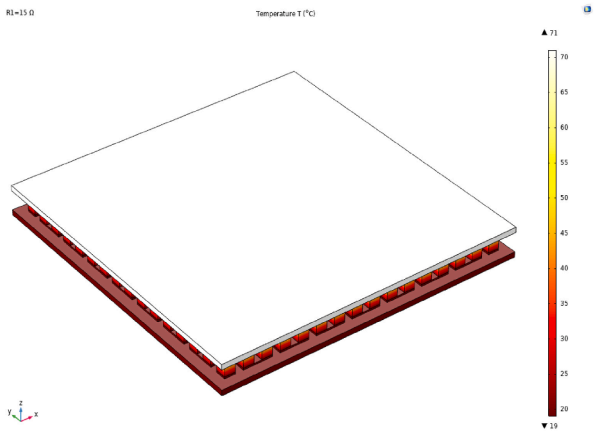

Fig. 6. Temperature distribution across the 1-CTEG configuration obtained under boundary condition scenario (1), where constant temperatures of 71 °C and 19 °C were applied to the top and bottom sides.

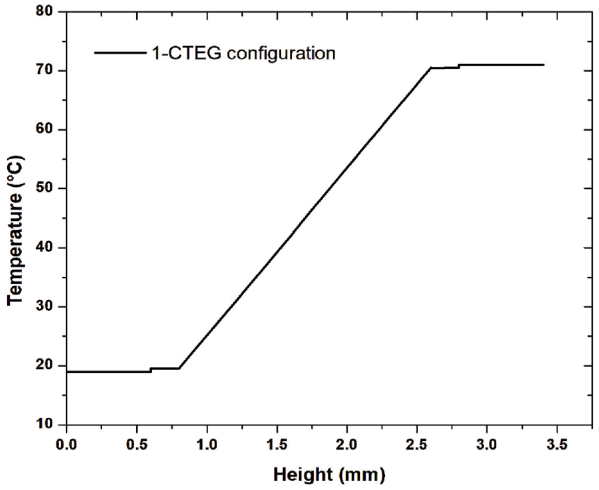

Fig. 7. Temperature variation across the 1-CTEG configuration obtained under boundary condition scenario (1), where constant temperatures of 71 °C and 19 °C were applied to the top and bottom sides.

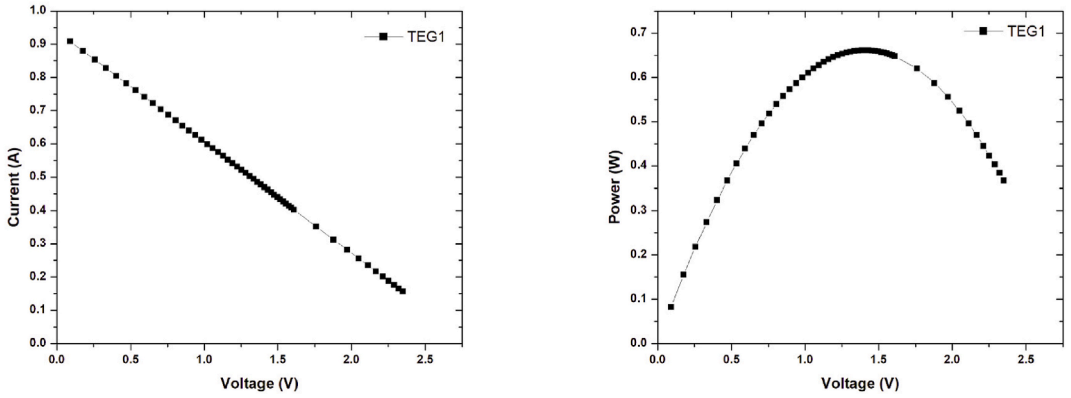

Fig. 8. I-V and P-V curves of the TEG1 component of the 1-CTEG configuration under boundary condition scenario (1), where constant temperatures of 71 °C and 19 °C were applied to the top and bottom sides.

Comparing the simulation results with the experimental data, I_{sc} was 23.6 % lower, while V_{oc} and P_{max} were 42.4 % and 35.4 % higher, respectively (refer to Table 7). There was a significant disparity between the simulation results and experimental data regarding these electrical parameters. This difference may stem from the nonuniform temperature distribution on the top and bottom sides of the 1-CTEG configuration, which was not accounted for in the numerical model. This nonuniform temperature distribution will be

Table 7
I_{sc}, V_{oc}, and P_{max} values extracted from the I-V and P-V curves of the TEG1 component of the 1-CTEG configuration under boundary condition scenario (1), where constant temperatures of 71 °C and 19 °C were applied to the top and bottom sides.

	Config.	Compon.	T_h (°C)	T_c (°C)	I_{sc} (A)	V_{oc} (V)	P_{max} (W)
Experiment	1-CTEG	TEG1	71.5	18.8	1.189	1.648	0.488
Simulation	1-CTEG	TEG1	71	19	0.908 (−23.6 %)	2.347 (+42.4 %)	0.661 (+35.4 %)

addressed in the boundary condition scenarios (2) and (3), where a circular pattern of temperature variation will be proposed for the top and bottom sides of the 1-CTEG configuration.

- 2-CTEG Configuration

The performance of the 2-CTEG configuration under boundary condition scenario (1) was explored. According to Table 5, the temperatures measured on the top and bottom sides of the 2-CTEG configuration were 109.4 °C and 18.8 °C, respectively. These values were used as inputs for the numerical model designed to simulate the 2-CTEG configuration under boundary conditions (1), where constant temperatures of 109 °C (≈109.4 °C) and 19 °C (≈18.8 °C) were applied to the top and bottom sides, respectively. The TEG1 and TEG2 components of the 2-CTEG configuration were connected to variable electrical resistors, enabling the analysis of their respective I-V and P-V curves separately.

Fig. 9 illustrates the resulting temperature distribution across the 2-CTEG configuration under these specified conditions. Fig. 10 depicts the temperature variation across the TEG1 component, thermally conductive tape, and TEG2 component, from top to bottom. This variation is linear across the p-type (or n-type) legs of both TEG1 and TEG2 due to their high thermal resistance,

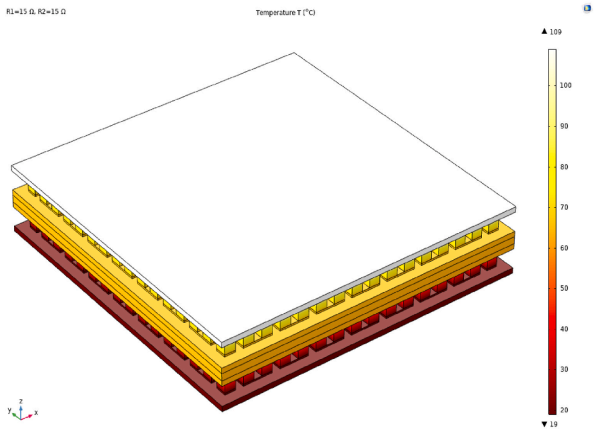

Fig. 9. Temperature distribution across the 2-CTEG configuration obtained under boundary condition scenario (1), where constant temperatures of 109 °C and 19 °C were applied to the top and bottom sides.

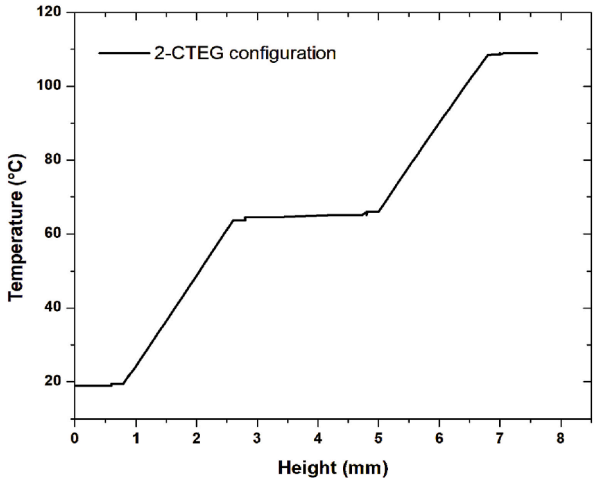

Fig. 10. Temperature variation across the 2-CTEG configuration obtained under boundary condition scenario (1), where constant temperatures of 109 °C and 19 °C were applied to the top and bottom sides.

while it remains almost constant across the alumina ceramics plates, thermally conductive tape, and copper interconnectors due to their high thermal conductivities. According to Fig. 10, the temperature differences across TEG1 and TEG2 were 43.9 °C and 45.5 °C, respectively. Therefore, both TEG1 and TEG2 almost evenly divide the total applied temperature difference ($\Delta T \approx 90$ °C), with each receiving approximately half of this total ($\Delta T_{1,2} \approx 45$ °C). This almost even temperature difference across TEG1 and TEG2 is due to their identical characteristics, which will result in TEG1 and TEG2 providing nearly identical I_{sc}, V_{oc}, and P_{max} values, as will be seen later.

Fig. 11 illustrates the I-V and P-V curves of the TEG1 and TEG2 components of the 2-CTEG configuration, while the I_{sc}, V_{oc}, and P_{max} values extracted from these curves are presented in Table 8.

Compared to the experiment results, I_{sc} was 9.7 % lower for TEG1, while V_{oc} and P_{max} were 32.1 % and 48.6 % higher, respectively. For TEG2, I_{sc} was 38.3 % lower, while V_{oc} and P_{max} were 39.9 % and 10.1 % higher, respectively (refer to Table 8). The simulation results significantly differ from the experimental data regarding these electrical parameters. This disparity may be attributed to the nonuniform temperature distribution on the top and bottom sides of the 2-CTEG configuration, which was not considered in the

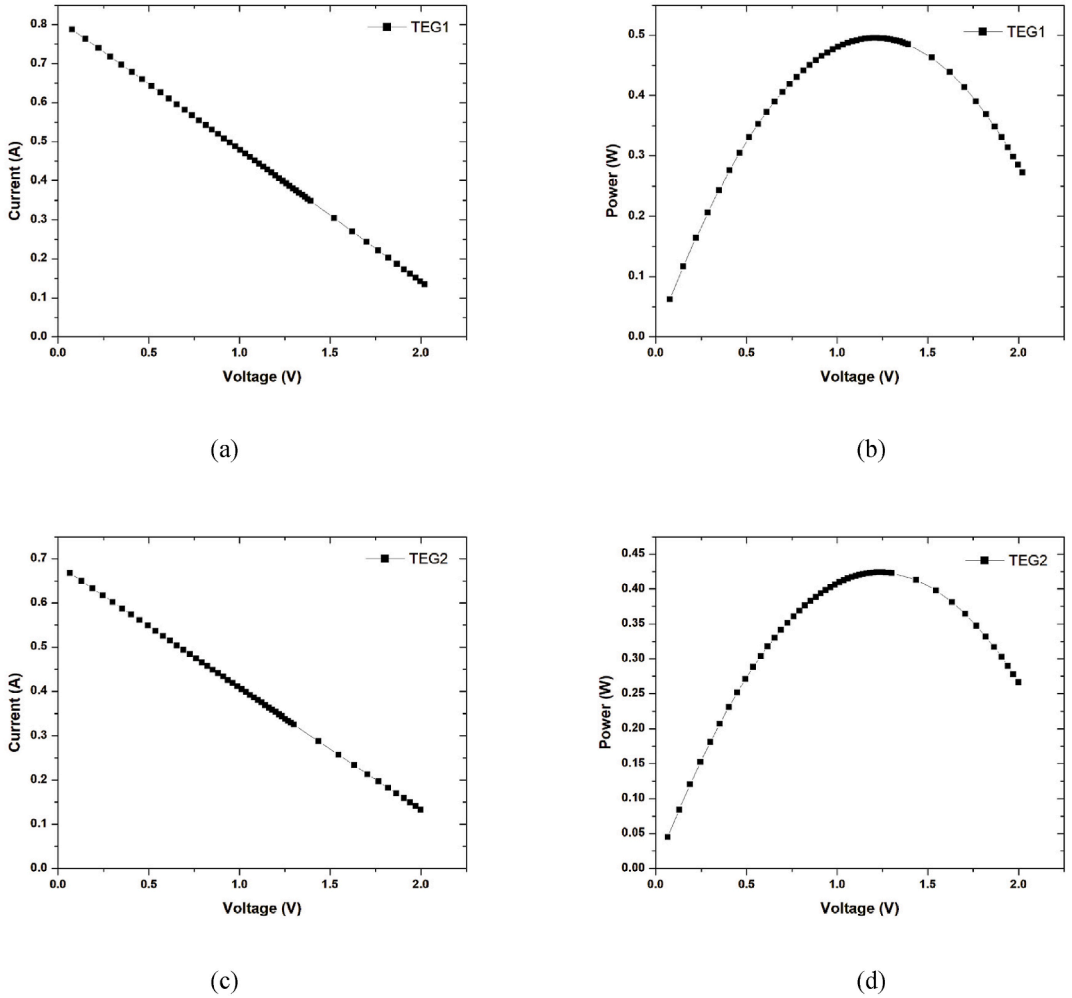

Fig. 11. I-V and P-V curves of TEG1 and TEG2 components of the 2-CTEG configuration under boundary condition scenario (1), where constant temperatures of 109 °C and 19 °C were applied to the top and bottom sides, showing: a) I-V curve for TEG1, b) P-V curve for TEG1, c) I-V curve for TEG2, and d) P-V curve for TEG2.

Table 8
I_{sc}, V_{oc}, and P_{max} values extracted from the I-V and P-V curves of the TEG1 and TEG2 components of the 2-CTEG configuration under boundary condition scenario (1), where constant temperatures of 109 °C and 19 °C were applied to the top and bottom sides.

	Config.	Compon.	T_h (°C)	T_c (°C)	I_{sc} (A)	V_{oc} (V)	P_{max} (W)
Experiment	2-CTEG	TEG1	109.4	66.7	0.873	1.529	0.333
		TEG2	66.7	18.8	1.082	1.428	0.385
Simulation	2-CTEG	TEG1	109	–	0.788 (−9.7 %)	2.020 (+32.1 %)	0.495 (+48.6 %)
		TEG2	–	19	0.667 (−38.3 %)	1.999 (+39.9 %)	0.424 (+10.1 %)

numerical model. This nonuniform temperature distribution will be addressed in boundary condition scenarios (2) and (3), where a circular pattern of temperature variations will be proposed for the top and bottom sides of the 2-CTEG configuration.

Additionally, TEG1 and TEG2 provide nearly identical I_{sc}, V_{oc}, and P_{max} values, with minor differences arising from the slightly uneven temperature difference across each one, as discussed earlier.

- 3-CTEG Configuration

The performance of the 3-CTEG configuration under boundary condition scenario (1) was also investigated. According to Table 6, the temperatures measured on the top and bottom sides of the 3-CTEG configuration are 107.7 ˚C and 16.9 ˚C, respectively. These values served as inputs for the numerical model designed to simulate the 3-CTEG configuration under boundary conditions (1), where constant temperatures of 108 ˚C (≈107.7 ˚C) and 17 ˚C (≈16.9 ˚C) were applied to the top and bottom sides, respectively. The three TEG components of the 3-CTEG configuration were connected to variable electrical resistors, enabling the analysis of their respective I-V and P-V curves separately.

Fig. 12 illustrates the resulting temperature distribution across the 3-CTEG configuration under these specified conditions. Fig. 13 illustrates the temperature variation across the TEG1 component, thermally conductive tape, TEG2 component, thermally conductive tape, and TEG3 component, from top to bottom. The temperature varies linearly across the p-type (or n-type) legs of TEG1, TEG2, and TEG3 due to their high thermal resistance, while it remains almost constant across the alumina ceramics plates, thermally conductive tapes, and copper interconnectors due to their high thermal conductivities. According to Fig. 13, the temperature differences across TEG1, TEG2, and TEG3 were 29.1 ˚C, 30.8 ˚C, and 30.4 ˚C, respectively. Therefore, TEG1, TEG2, and TEG3 almost equally divide the total applied temperature difference ($\Delta T \approx 91$ ˚C), with each receiving nearly one-third of this total ($\Delta T_{1,2,3} \approx 30$ ˚C). This almost even temperature difference across TEG1, TEG2, and TEG3 is due to their identical characteristics, which will result in TEG1, TEG2, and TEG3 providing nearly identical I_{sc}, V_{oc}, and P_{max} values, as will be seen later.

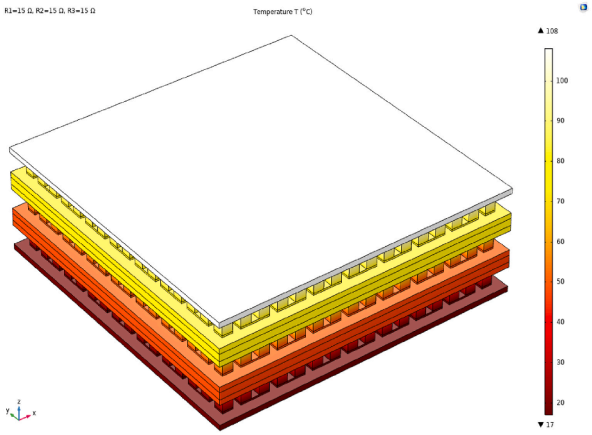

Fig. 12. Temperature distribution across the 3-CTEG configuration obtained under boundary condition scenario (1), where constant temperatures of 108 ˚C and 17 ˚C were applied to the top and bottom sides.

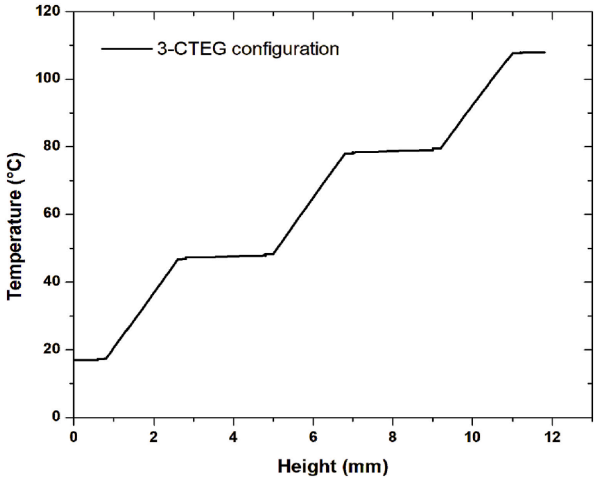

Fig. 13. Temperature variation across the 3-CTEG configuration obtained under boundary condition scenario (1), where constant temperatures of 108 ˚C and 17 ˚C were applied to the top and bottom sides.

Fig. 14 illustrates the I-V and P-V curves of the TEG1, TEG2, and TEG3 components of the 3-CTEG configuration, while the I_{sc}, V_{oc}, and P_{max} values extracted from these curves are presented in Table 9.

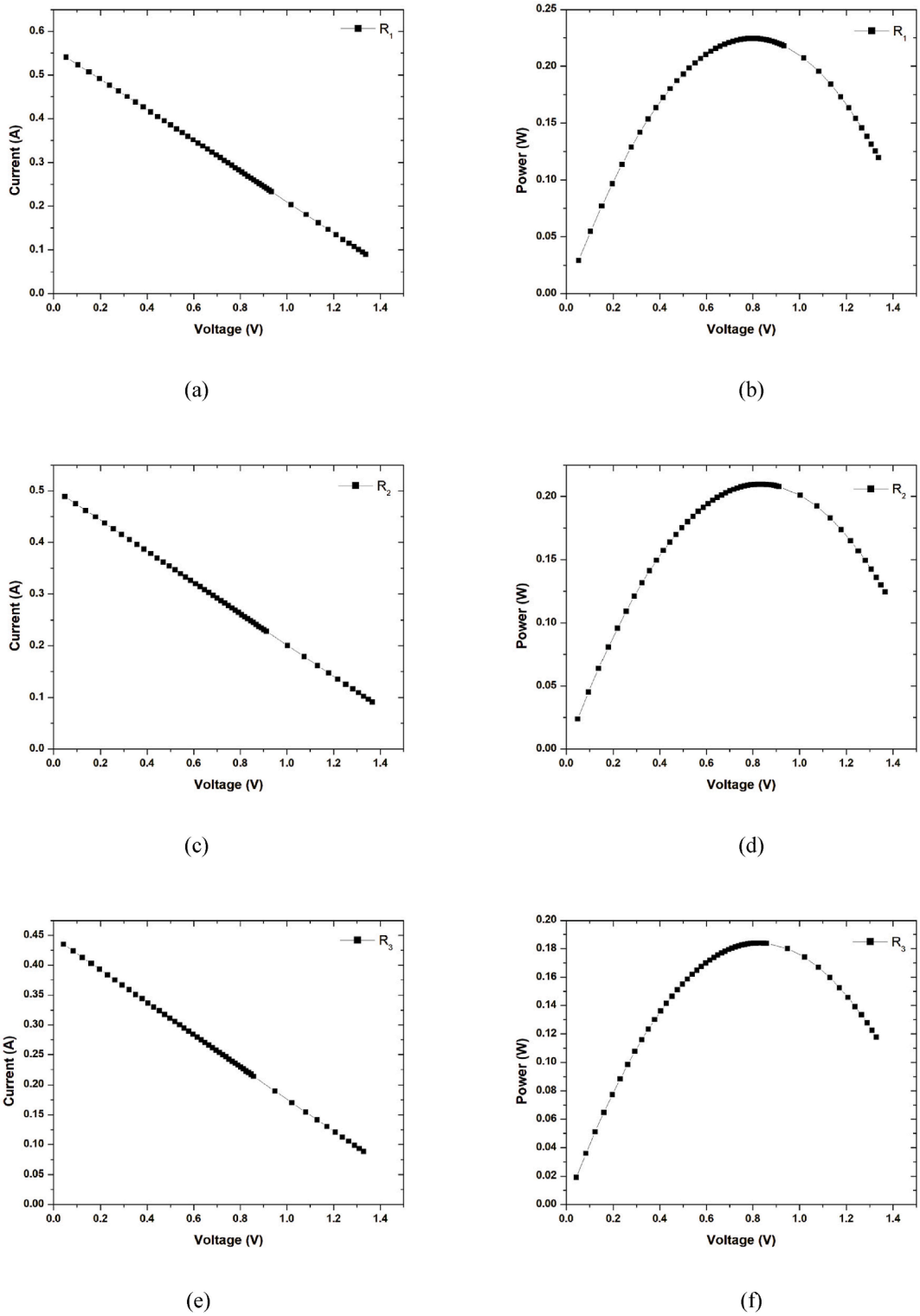

Fig. 14. I-V and P-V curves of TEG1, TEG2 and TEG3 components of the 3-CTEG configuration under boundary condition scenario (1), where constant temperatures of 108 °C and 17 °C were applied to the top and bottom sides, showing: a) I-V curve for TEG1, b) P-V curve for TEG1, c) I-V curve for TEG2, d) P-V curve for TEG2, e) I-V curve for TEG3, and f) P-V curve for TEG3.

Table 9
I_{sc}, V_{oc}, and P_{max} values extracted from the I-V and P-V curves of the TEG1, TEG2, and TEG3 components of the 3-CTEG configuration under boundary condition scenario (1), where constant temperatures of 108 °C and 17 °C were applied to the top and bottom sides.

	Config.	Compon.	T_h (°C)	T_c (°C)	I_{sc} (A)	V_{oc} (V)	P_{max} (W)
Experiment	3-CTEG	TEG1	107.7	78.6	0.479	1.079	0.129
		TEG2	78.6	46.9	0.675	0.988	0.166
		TEG3	46.9	16.9	0.735	0.905	0.166
Simulation	3-CTEG	TEG1	108	–	0.541 (+12.9 %)	1.338 (+24.0 %)	0.224 (+73.6 %)
		TEG2	–	–	0.489 (−27.5 %)	1.365 (+38.1 %)	0.210 (+26.5 %)
		TEG3	–	17	0.435 (−40.8 %)	1.328 (+46.7 %)	0.184 (+10.8 %)

Compared to the experimental results, I_{sc}, V_{oc}, and P_{max} were 12.9 %, 24.0 %, and 73.6 % higher, respectively, for TEG1. For TEG2, I_{sc} was 27.5 % lower, while V_{oc}, and P_{max} were 38.1 % and 26.5 % higher, respectively. Regarding TEG3, I_{sc} was 40.8 % lower, while V_{oc}, and P_{max} were 46.7 % and 10.8 % higher, respectively (refer to Table 9). Therefore, there is a notable disparity between the simulated and experimental results concerning these electrical parameters, possibly due to the nonuniform temperature distribution on the top and bottom sides of the 3-CTEG configuration, which was not considered in the simulation. This nonuniform temperature distribution will be addressed in boundary condition scenarios (2) and (3), where a circular pattern of temperature variation will be proposed for the top and bottom sides of the 3-CTEG configuration.

Additionally, TEG1, TEG2, and TEG3 provide nearly identical I_{sc}, V_{oc}, and P_{max} values, with minor differences arising from the slightly uneven temperature difference across each one, as discussed earlier.

3.2.2. Scenario (2): circular pattern of temperature variation on the top side with constant temperature on the bottom side

- 1-CTEG Configuration

The performance of the 1-CTEG configuration under boundary condition scenario (2) was explored, assuming a nonuniform temperature distribution on the top side of the 1-CTEG configuration due to nonuniform solar irradiance, while maintaining a uniform temperature distribution on the bottom side due to a perfect heat sink. A circular pattern of temperature variation was suggested, featuring a central circular region surrounded by thick, same-width concentric rings, as shown in Fig. 15. The circular pattern exhibits the highest temperature at the central region, gradually decreasing with a specific decrement across the surrounding rings and remaining part of the top-side surface. Two combinations of decrements for temperature variation were considered in the simulations. The first combination involved a decrement of 1 across the central region, surrounding rings, and remaining part of the top-side surface, while the second combination had a decrement of 1 across the central region and the first and second surrounding rings, and a decrement of 2 across the remaining surrounding rings and the remaining part.

The rationale behind the proposed circular pattern of temperature variation is based on the nonuniform high solar irradiance to which the PV-TEG hybrid system coupling TEG to PV cell is exposed [57]. This nonuniform irradiance results in uneven thermal energy conduction between the PV cell and the TEG, leading to a nonuniform temperature variation on the hot side of the TEG [58]. Additionally, the suggested circular pattern of temperature variation was demonstrated by Fallah Kohan et al. in their study on the numerical simulation of a photovoltaic thermoelectric hybrid power generation system [41].

The measured temperatures for the top and bottom sides of the 1-CTEG configuration were 71.5 °C and 18.8 °C, respectively (refer to Table 4). These temperatures were recorded at the center of the top-side and bottom-side surfaces and utilized as reference inputs for the numerical model designed to simulate the 1-CTEG configuration under boundary condition scenarios (2) and (3). In the cur-

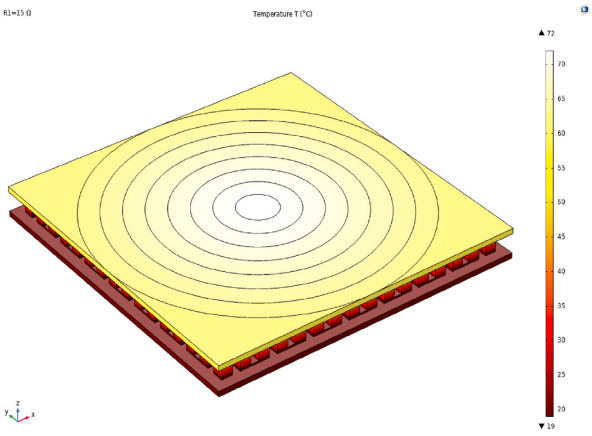

Fig. 15. Temperature distribution across the 1-CTEG configuration under boundary condition scenario (2), where a circular pattern of temperature variation, with temperatures of 72, 71, 70, 68, 66, 64, 62, 60, and 58 °C, was applied to the top side and a constant temperature of 19 °C was applied to the bottom side.

rent scenario, a constant temperature of 19 °C (≈18.8 °C) was applied to the bottom side, while two sets of temperatures (72, 71, 70, 69, 68, 67, 66, 65, 64 °C and 72, 71, 70, 68, 66, 64, 62, 60, 58 °C) were applied to the top side.

Fig. 15 illustrates the resulting temperature distribution across the 1-CTEG configuration under boundary condition scenario (2), where a circular pattern of temperature variation (72, 71, 70, 68, 66, 64, 62, 60, 58 °C) was applied to the top side and a constant temperature of 19 °C was applied to the bottom side. The I-V and P-V curves of the TEG1 component of the 1-CTEG configuration under the current scenario are not presented to avoid making the manuscript heavier. However, Table 10 presents the I_{sc}, V_{oc}, and P_{max} values extracted from these curves.

Comparing the simulated results to the experimental results, it was observed that the second set of boundary conditions, with temperatures of 72, 71, 70, 68, 66, 64, 62, 60, and 58 °C applied to the top side and a constant temperature of 19 °C applied to the bottom side, yielded the closest results. Particularly for P_{max}, which was only 1.0 % lower compared to the measured value, despite the simulated I_{sc} and V_{oc} being 34.0 % lower and 21.0 % higher, respectively.

- 2-CTEG Configuration

The performance of the 2-CTEG configuration under boundary condition scenario (2) was also explored, assuming a nonuniform temperature distribution on the top side of the 2-CTEG configuration due to nonuniform solar irradiance, while maintaining a uniform temperature distribution on the bottom side due to a perfect heat sink.

Similarly, the proposed circular pattern was also employed for simulating the 2-CTEG configuration under boundary conditions scenario (2). The circular pattern was exclusively applied to the top side, while a constant temperature was applied to the bottom side. The two combinations of decrements for temperature variation were also considered in the simulations.

The measured temperatures for the top and bottom sides of the 2-CTEG configuration were 109.4 °C and 18.8 °C, respectively (refer to Table 5). These temperatures were recorded at the center of the top-side and bottom-side surfaces and utilized as reference inputs for the numerical model designed to simulate the 2-CTEG configuration under boundary condition scenarios (2) and (3). In the current scenario, a constant temperature of 19 °C (≈18.8 °C) was applied to the bottom side, while two sets of temperatures (109, 108, 107, 106, 105, 104, 103, 102, 101 °C and 109, 108, 107, 105, 103, 101, 99, 97, 95 °C) were applied to the top side.

Fig. 16 illustrates the resulting temperature distribution across the 2-CTEG configuration under boundary condition scenario (2), where a circular pattern of temperature variation, with temperatures of 109, 108, 107, 105, 103, 101, 99, 97, and 95 °C, was applied to the top side and a constant temperature of 19 °C was applied to the bottom side. Table 11 presents the I_{sc}, V_{oc}, and P_{max} values extracted from the I-V and P-V curves of the TEG1 and TEG2 components.

Referring to Tables 11 and it was challenging to make direct comparisons between the simulated and experimental results due to the high number of electrical parameter results (I_{sc}, V_{oc}, and P_{max}) provided by the TEG components of the 2-CTEG configuration and for two simulated sets of temperatures. Therefore, the comparisons between the simulated and experimental results were exclusively

Table 10
I_{sc}, V_{oc}, and P_{max} values extracted from the I-V and P-V curves of the TEG1 component of the 1-CTEG configuration under boundary condition scenario (2), where a circular pattern of temperature variation, with two different temperature sets, was applied to the top side and a constant temperature of 19 °C was applied to the bottom side.

	Config.	Compon.	T_h (°C)	T_c (°C)	I_{sc} (A)	V_{oc} (V)	P_{max} (W)
Experience	1-CTEG	TEG1	71.5	18.8	1.189	1.648	0.488
Simulation	1-CTEG	TEG1	72; 71; 70; 69; 68; 67; 66; 65; 64	19	0.838 (−29.5 %)	2.150 (+30.5 %)	0.558 (−14.3 %)
		TEG1	72; 71; 70; 68; 66; 64; 62; 60; 58	19	0.782 (−34.0 %)	1.996 (+21.0 %)	0.483 (−1.0 %)

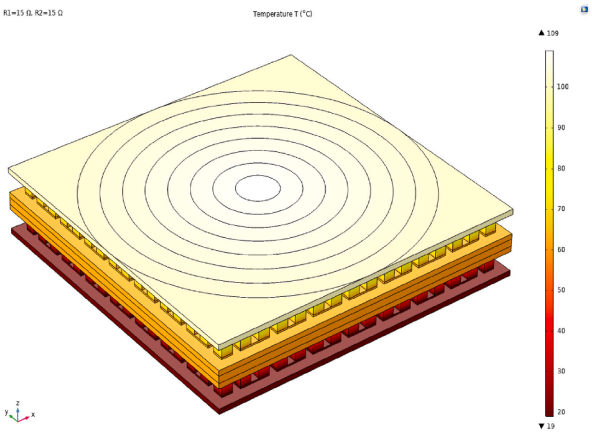

Fig. 16. Temperature distribution across the 2-CTEG configuration under boundary condition scenario (2), where a circular pattern of temperature variation, with temperatures of 109, 108, 107, 105, 103, 101, 99, 97, and 95 °C, was applied to the top side and a constant temperature of 19 °C was applied to the bottom side.

Table 11
I_{sc}, V_{oc}, and P_{max} values extracted from the I-V and P-V curves of the TEG1 and TEG2 components of the 2-CTEG configuration under boundary condition scenario (2), where a circular pattern of temperature variation, with two different temperature sets, was applied to the top side and a constant temperature of 19 °C was applied to the bottom side.

	Config.	Compon.	T_h (°C)	T_c (°C)	I_{sc} (A)	V_{oc} (V)	P_{max} (W)	Total P_{max} (W)
Experiment	2-CTEG	TEG1	109.4	66.7	0.873	1.529	0.333	0.718
		TEG2	66.7	18.8	1.082	1.428	0.385	
Simulation	2-CTEG	TEG1	109; 108; 107; 106; 105; 104; 103; 102; 101	–	0.742 (−15.0 %)	1.893 (+24.0 %)	0.437 (+31.0 %)	0.816 (+13.6 %)
		TEG2	–	19	0.636 (−41.0 %)	1.884 (+32.0 %)	0.379 (−1.5 %)	
		TEG1	109; 108; 107; 105; 103; 101; 99; 97; 95	–	0.713 (−18.3 %)	1.813 (+18.6 %)	0.402 (+20.7 %)	0.754 (+5.0 %)
		TEG2	–	19	0.616 (−43.1 %)	1.811 (+26.8 %)	0.352 (−8.6 %)	

focused on the total P_{max}, which is the sum of the P_{max} values provided by TEG1 and TEG2, as presented in the last column of Table 11.

Comparing the simulated and experimental total P_{max}, it was observed that the circular pattern, with temperatures of 109, 108, 107, 105, 103, 101, 99, 97, and 95 °C applied to the top side and a constant temperature of 19 °C applied to the bottom side, yielded the closest total P_{max}, being 5.0 % higher compared to the experimental value.

- 3-CTEG Configuration

The performance of the 3-CTEG configuration under boundary condition scenario (2) was also explored, assuming a nonuniform temperature distribution on the top side of the 3-CTEG configuration due to nonuniform solar irradiance, while maintaining a uniform temperature distribution on the bottom side due to a perfect heat sink.

Fig. 17 illustrates the resulting temperature distribution across the 3-CTEG simulated under boundary condition scenario (2), where a circular pattern of temperature variation, with temperatures of 108, 107, 106, 104, 102, 100, 98, 96, and 94 °C, was applied to the top side and a constant temperature of 17 °C was applied to the bottom side. Table 12 presents the I_{sc}, V_{oc}, and P_{max} values extracted from the I-V and P-V curves of the TEG1, TEG2, and TEG3 components.

Referring to Tables 12 and it was challenging to make direct comparisons between the simulated and experimental results due to the high number of electrical parameter results (I_{sc}, V_{oc}, and P_{max}) provided by the TEG components of the 3-CTEG configuration and for two simulated sets of temperatures. Therefore, the comparisons between the simulated and experimental results were exclusively focused on the total P_{max}, which is the sum of the P_{max} values provided by TEG1, TEG2, and TEG3, as presented in the last column of Table 12.

Comparing the simulated and experimental total P_{max}, it was observed that the circular pattern, with temperatures of 108, 107, 106, 104, 102, 100, 98, 96, and 94 °C applied to the top side and a constant temperature of 17 °C applied to the bottom side, yielded the closest total P_{max}, being 10.2 % higher compared to the experimental value.

3.2.3. Scenario (3): circular pattern of temperature variation on both the top and bottom sides

- 1-CTEG Configuration

The performance of the 1-CTEG configuration under boundary condition scenario (3) was investigated, assuming a nonuniform temperature distribution on both the top and bottom sides of the 1-CTEG configuration due to nonuniform solar irradiance and an im-

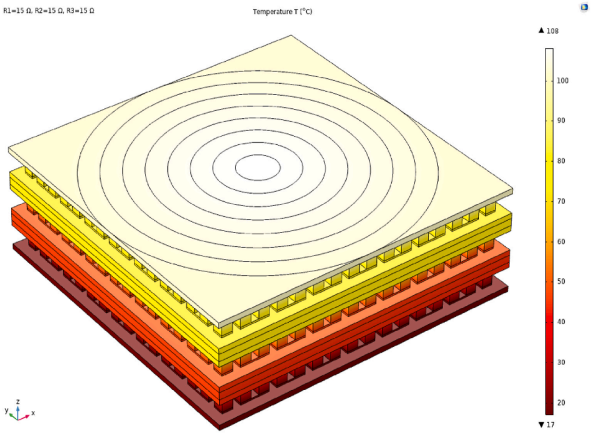

Fig. 17. Temperature distribution across the 3-CTEG configuration under boundary condition scenario (2), where a circular pattern of temperature variation, with temperatures of 108, 107, 106, 104, 102, 100, 98, 96, and 94 °C, was applied to the top side and a constant temperature of 17 °C was applied to the bottom side.

Table 12
I_{sc}, V_{oc}, and P_{max} values extracted from the I-V and P-V curves of the TEG1, TEG2, and TEG3 components of the 3-CTEG configuration under boundary condition scenario (2), where a circular pattern of temperature variation, with two different temperature sets, was applied to the top side and a constant temperature of 17 °C was applied to the bottom side.

	Config.	Compon.	T_h (°C)	T_c (°C)	I_{sc} (A)	V_{oc} (V)	P_{max} (W)	Total P_{max} (W)
Experiment	3-CTEG	TEG1	107.7	78.6	0.479	1.079	0.129	0.461
		TEG2	78.6	46.9	0.675	0.988	0.166	
		TEG3	46.9	16.9	0.735	0.905	0.166	
Simulation	3-CTEG	TEG1	108; 107; 106; 105; 104; 103; 102; 101; 100	–	0.509 (+6.26 %)	1.254 (+16.2 %)	0.198 (+53.5 %)	0.549 (+19.1 %)
		TEG2	–	–	0.464 (−31.2 %)	1.283 (+29.8 %)	0.186 (+12.0 %)	
		TEG3	–	17	0.416 (−43.4 %)	1.255 (+38.7 %)	0.165 (−0.6 %)	
		TEG1	108; 107; 106; 104; 102; 100; 98; 96; 94	–	0.489 (+2.1 %)	1.202 (+11.4 %)	0.182 (+41.1 %)	0.508 (+10.2 %)
		TEG2	–	–	0.447 (−33.8 %)	1.231 (+24.6 %)	0.172 (+3.6 %)	
		TEG3	–	17	0.403 (−45.2 %)	1.207 (+33.4 %)	0.154 (−7.2 %)	

perfect heat sink, respectively. The proposed circular pattern of temperature variation was applied to both the top and bottom sides of the 1-CTEG configuration.

Considering the minor temperature nonuniformity on the bottom side of the 1-CTEG configuration compared to the top side, the temperature decrement across the bottom side was set to 0.1. This approach provided a single set of temperatures (18.8, 18.7, 18.6, 18.5, 18.4, 18.3, 18.2, 18.1, and 18.0 °C) for the circular pattern applied to the bottom side. For the circular pattern applied to the top side, the two sets of temperatures (72, 71, 70, 69, 68, 67, 66, 65, 64 °C and 72, 71, 70, 68, 66, 64, 62, 60, 58 °C) used under boundary condition scenario (2) were employed. Table 13 presents the I_{sc}, V_{oc}, and P_{max} values extracted from the I-V and P-V curves of the TEG1 component.

Comparing the simulated and experimental results, it was observed that the circular pattern with temperatures of 72, 71, 70, 68, 66, 64, 62, 60, and 58 °C applied to the top side and temperatures of 18.8, 18.7, 18.6, 18.5, 18.4, 18.3, 18.2, 18.1, and 18.0 °C applied to the bottom side yielded the closest P_{max}, being 2.4 % higher compared to the experimental P_{max}.

- 2-CTEG Configuration

The performance of the 2-CTEG configuration under boundary condition scenario (3) was investigated, assuming a nonuniform temperature distribution on both the top and bottom sides of the 2-CTEG configuration due to nonuniform solar irradiance and an imperfect heat sink, respectively. The proposed circular pattern of temperature variation was applied to both the top and bottom sides of the 2-CTEG configuration.

Considering the minor temperature nonuniformity on the bottom side of the 2-CTEG configuration compared to the top side, the temperature decrement across the bottom side was set to 0.1. This approach provided a single set of temperatures (18.8, 18.7, 18.6, 18.5, 18.4, 18.3, 18.2, 18.1, and 18.0 °C) for the circular pattern applied to the bottom side. For the circular pattern applied to the top side, the two sets of temperatures (109, 108, 107, 106, 105, 104, 103, 102, 101 °C and 109, 108, 107, 105, 103, 101, 99, 97, 95 °C) used under boundary condition scenario (2) were employed. Table 14 presents the I_{sc}, V_{oc}, and P_{max} values extracted from the I-V and P-V curves of the TEG1 and TEG2 components.

Comparing the simulated and experimental total P_{max}, it was observed that the circular pattern with temperatures of 109, 108, 107, 105, 103, 101, 99, 97, and 95 °C applied to the top side and temperatures of 18.8, 18.7, 18.6, 18.5, 18.4, 18.3, 18.2, 18.1, and 18.0 °C applied to the bottom side yielded the closest total P_{max}, being 7.1 % higher compared to the experimental total P_{max}. Additionally, the TEG1 and TEG2 components yielded nearly identical simulation results, with a negligible difference attributed to the slight variation in temperature difference across each one.

- 3-CTEG Configuration

The performance of the 3-CTEG configuration under boundary condition scenario (3) was investigated, assuming a nonuniform temperature distribution on both the top and bottom sides of the 3-CTEG configuration due to nonuniform solar irradiance and an imperfect heat sink, respectively. The proposed circular pattern of temperature variation was applied to both the top and bottom sides of the 3-CTEG configuration.

Table 13
I_{sc}, V_{oc}, and P_{max} values extracted from the I-V and P-V curves of the TEG1 component of the 1-CTEG configuration under boundary condition scenario (3), where a circular pattern with two temperature sets was applied to the top side and a single temperature set was applied to the bottom side.

	Config.	Compon.	T_h (°C)	T_c (°C)	I_{sc} (A)	V_{oc} (V)	P_{max} (W)
Experience	1-CTEG	TEG1	71.5	18.8	1.189	1.648	0.488
Simulation	1-CTEG	TEG1	72; 71; 70; 69; 68; 67; 66; 65; 64	18.8; 18.7; 18.6; 18.5; 18.4; 18.3; 18.2; 18.1; 18.0	0.851 (−28.4 %)	2.182 (+32.4 %)	0.576 (+18.0 %)
		TEG1	72; 71; 70; 68; 66; 64; 62; 60; 58	18.8; 18.7; 18.6; 18.5; 18.4; 18.3; 18.2; 18.1; 18.0	0.796 (−33.0 %)	2.028 (+23.0 %)	0.500 (+2.4 %)

Table 14
I_{sc}, V_{oc}, and P_{max} values extracted from the I-V and P-V curves of the TEG1 and TEG2 components of the 2-CTEG configuration under boundary condition scenario (3), where a circular pattern with two sets of temperatures was applied to the top side and a single set of temperatures was applied to the bottom side.

	Config.	Compon.	T_h (°C)	T_c (°C)	I_{sc} (A)	V_{oc} (V)	P_{max} (W)	Total P_{max} (W)
Experiment	2-CTEG	TEG1	109.4	66.7	0.873	1.529	0.333	0.718
		TEG2	66.7	18.8	1.082	1.428	0.385	
Simulation	2-CTEG	TEG1	109; 108; 107; 106; 105; 104; 103; 102; 101	–	0.750 (−14.1 %)	1.908 (+24.8 %)	0.445 (+33.6 %)	0.832 (+15.9 %)
		TEG2	–	18.8; 18.7; 18.6; 18.5; 18.4; 18.3; 18.2; 18.1; 18.0	0.642 (−40.7 %)	1.901 (+33.1 %)	0.387 (+0.5 %)	
		TEG1	109; 108; 107; 105; 103; 101; 99; 97; 95	–	0.721 (−17.4 %)	1.828 (+19.5 %)	0.409 (+22.8 %)	0.769 (+7.1 %)
		TEG2	–	18.8; 18.7; 18.6; 18.5; 18.4; 18.3; 18.2; 18.1; 18.0	0.622 (−42.5 %)	1.828 (+28.0 %)	0.360 (+8.1 %)	

Considering the minor temperature nonuniformity on the bottom side of the 3-CTEG configuration compared to the top side, the temperature decrement across the bottom side was set to 0.1. This approach provided a single set of temperatures (16.9, 16.8, 16.7, 16.6, 16.5, 16.4, 16.3, 16.2, and 16.1 °C) for the circular pattern applied to the bottom side. For the circular pattern applied to the top side, the two sets of temperatures (108, 107, 106, 105, 104, 103, 102, 101, 100 °C and 108, 107, 106, 104, 102, 100, 98, 96, 94 °C) used under boundary condition scenario (2) were employed. Table 15 presents the I_{sc}, V_{oc}, and P_{max} values extracted from the I-V and P-V curves of the TEG1, TEG2, and TEG3 components.

Comparing the simulated and experimental total P_{max}, it was observed that the circular pattern with temperatures of 108, 107, 106, 104, 102, 100, 98, 96, and 94 °C applied to the top side and temperatures of 16.9, 16.8, 16.7, 16.6, 16.5, 16.4, 16.3, 16.2, and 16.1 °C applied to the bottom side yielded the closest total P_{max}, being 11.9 % higher compared to the experimental total P_{max}. Additionally, the TEG1, TEG2, and TEG3 components yielded nearly identical simulation results, with a negligible difference attributed to the slight variation in temperature difference across each one.

3.2.4. Comparison between scenarios (1)–(3)

When comparing total P_{max} for the 1-CTEG configuration under scenarios (1)–(3) with the experimental total P_{max}, the results were 35.4 % higher under scenario (1), 1.0 % lower under scenario (2), and 2.4 % higher under scenario (3). It was evident that scenario (2) aligns more closely with the experimental results compared to scenarios (1) and (3) (refer to Table 16).

When comparing total P_{max} for the 2-CTEG configuration under scenarios (1)–(3) with the experimental total P_{max}, the results were 28.0 % higher under scenario (1), 5.0 % higher under scenario (2), and 7.1 % higher under scenario (3). It was evident that scenario (2) aligns more closely with the experimental results compared to scenarios (1) and (3) (refer to Table 17).

When comparing total P_{max} for the 3-CTEG configuration under scenarios (1)–(3) with the experimental total P_{max}, the results were 34.0 % higher under scenario (1), 10.2 % higher under scenario (2), and 11.9 % higher under scenario (3). It was evident that scenario (2) aligns more closely with the experimental results compared to scenarios (1) and (3) (refer to Table 18).

Table 15
I_{sc}, V_{oc}, and P_{max} values extracted from the I-V and P-V curves of the TEG1, TEG2, and TEG3 components of the 3-CTEG configuration under boundary condition scenario (3), where a circular pattern with two sets of temperatures was applied to the top side and a single set of temperatures was applied to the bottom side.

	Config.	Compon.	T_h (°C)	T_c (°C)	I_{sc} (A)	V_{oc} (V)	P_{max} (W)	Total P_{max} (W)
Experiment	3-CTEG	TEG1	107.7	78.6	0.479	1.079	0.129	0.461
		TEG2	78.6	46.9	0.675	0.988	0.166	
		TEG3	46.9	16.9	0.735	0.905	0.166	
Simulation	3-CTEG	TEG1	108; 107; 106; 105; 104; 103; 102; 101; 100	–	0.513 (+7.1 %)	1.262 (+16.9 %)	0.201 (+55.8 %)	0.558 (+21.0 %)
		TEG2	–	–	0.467 (−30.8 %)	1.293 (+30.9 %)	0.189 (+13.8 %)	
		TEG3	–	16.9; 16.8; 16.7; 16.6; 16.5; 16.4; 16.3; 16.2; 16.1	0.419 (−43.0 %)	1.264 (+39.7 %)	0.168 (+1.2 %)	
		TEG1	108; 107; 106; 104; 102; 100; 98; 96; 94	–	0.493 (+2.9 %)	1.210 (+12.1 %)	0.185 (+43.4 %)	0.516 (+11.9 %)
		TEG2	–	–	0.451 (−33.2 %)	1.240 (+25.5 %)	0.175 (+5.4 %)	
		TEG3	–	16.9; 16.8; 16.7; 16.6; 16.5; 16.4; 16.3; 16.2; 16.1	0.406 (−44.7 %)	1.217 (+34.5 %)	0.156 (−6.0 %)	

Table 16
Comparison of simulated results for the 1-CTEG configuration under scenarios (1)–(3).

	Config.		Compon.	I_{sc} (A)	V_{oc} (V)	P_{max} (W)
Experiment	1-CTEG		TEG1	1.189	1.648	0.488
Simulation	1-CTEG	Scenario (1)	TEG1	0.908 (−23.6 %)	2.347 (+42.4 %)	0.661 (+35.4 %)
		Scenario (2)	TEG1	0.782 (−34.0 %)	1.996 (+21.0 %)	0.483 (−1.0 %)
		Scenario (3)	TEG1	0.796 (−33.0 %)	2.028 (+23.0 %)	0.500 (+2.4 %)

Table 17
Comparison of simulated results for the 2-CTEG configuration under scenarios (1)–(3).

	Config.		Compon.	I_{sc} (A)	V_{oc} (V)	P_{max} (W)	Total P_{max} (W)
Experiment	2-CTEG		TEG1	0.873	1.529	0.333	0.718
			TEG2	1.082	1.428	0.385	
Simulation	2-CTEG	Scenario (1)	TEG1	0.788 (−9.7 %)	2.020 (+32.1 %)	0.495 (+48.6 %)	0.919 (+28.0 %)
			TEG2	0.667 (−38.3 %)	1.999 (+39.9 %)	0.424 (+10.1 %)	
		Scenario (2)	TEG1	0.713 (−18.3 %)	1.813 (+18.6 %)	0.402 (+20.7 %)	0.754 (+5.0 %)
			TEG2	0.616 (−43.1 %)	1.811 (+26.8 %)	0.352 (−8.6 %)	
		Scenario (3)	TEG1	0.721 (−17.4 %)	1.828 (+19.5 %)	0.409 (+22.8 %)	0.769 (+7.1 %)
			TEG2	0.622 (−42.5 %)	1.828 (+28.0 %)	0.360 (+8.1 %)	

Table 18
Comparison of simulated results for the 3-CTEG configuration under scenarios (1)–(3).

	Config.		Compon.	I_{sc} (A)	V_{oc} (V)	P_{max} (W)	Total P_{max} (W)
Experiment	3-CTEG		TEG1	0.479	1.079	0.129	0.461
			TEG2	0.675	0.988	0.166	
			TEG3	0.735	0.905	0.166	
Simulation	3-CTEG	Scenario (1)	TEG1	0.541 (+12.9 %)	1.338 (+24.0 %)	0.224 (+73.6 %)	0.618 (+34.0 %)
			TEG2	0.489 (−27.5 %)	1.365 (+38.1 %)	0.210 (+26.5 %)	
			TEG3	0.435 (−40.8 %)	1.328 (+46.7 %)	0.184 (+10.8 %)	
		Scenario (2)	TEG1	0.489 (+2.1 %)	1.202 (+11.4 %)	0.182 (+41.1 %)	0.508 (+10.2 %)
			TEG2	0.447 (−33.8 %)	1.231 (+24.6 %)	0.172 (+3.6 %)	
			TEG3	0.403 (−45.2 %)	1.207 (+33.4 %)	0.154 (−7.2 %)	
		Scenario (3)	TEG1	0.493 (+2.9 %)	1.210 (+12.1 %)	0.185 (+43.4 %)	0.516 (+11.9 %)
			TEG2	0.451 (−33.2 %)	1.240 (+25.5 %)	0.175 (+5.4 %)	
			TEG3	0.406 (−44.7 %)	1.217 (+34.5 %)	0.156 (−6.0 %)	

3.2.5. Quantitative metrics

The Root Mean Square Error (RMSE) was utilized as a statistical measure to assess the agreement between simulation and experimental results across scenarios (1)–(3). The RMSE was calculated between the experimental and simulated total P_{max} results provided by the three CTEG configurations (1-CTEG, 2-CTEG, and 3-CTEG), as shown in Table 19. The calculated RMSE values for scenarios (1), (2), and (3) were 0.178, 0.034, and 0.044, respectively. A significant improvement in the RMSE value was observed for the simulated total P_{max} results obtained in scenario (2). Therefore, the matching between experimental and simulated total P_{max} results was found to be very good for scenario (2).

4. Conclusion

There has been significant interest in attaching CTEGs to the backside of solar cells exposed to high concentrated solar irradiance. This passive technique reduces the operating temperature of solar cells, maintaining their efficiency, and generates additional electrical energy through CTEGs. However, the nonuniform distribution of concentrated sunlight and imperfect cooling by heat sinks cause uneven temperature distributions on both sides of the CTEGs, impacting their efficiency. Understanding this temperature distribution is crucial for enhancing the performance of PV-CTEG hybrid systems.

Table 19
Calculated RMSE values between experimental and simulated total P_{max} results for the 1-CTEG, 2-CTEG, and 3-CTEG configurations across scenarios (1)–(3).

Config.	Experimental total P_{max} (W)	Simulated total P_{max} (W)		
		Scenario (1)	Scenario (2)	Scenario (3)
1-CTEG	0.488	0.661	0.483	0.500
2-CTEG	0.718	0.919	0.754	0.769
3-CTEG	0.461	0.618	0.508	0.516
RMSE	–	0.178	0.034	0.044

There is a significant gap in research concerning the investigation of temperature variation on the top and bottom sides of CTEGs in PV-CTEG hybrid systems. Unlike previous studies, which mainly employed either a single central circle with varying diameters or identical squares with the same dimensions to simulate these temperature variations on either the hot or cold sides of thermoelectric generators, the current paper explores a circular pattern of temperature variation. This pattern features a central circular region surrounded by thick, same-width concentric rings on the top and bottom sides of three CTEG configurations (1- CTEG, 2- CTEG, and 3-CTEG), in addition to a uniform temperature distribution.

Theoretically, using COMSOL Multiphysics, the three CTEG configurations were simulated under three distinct boundary condition scenarios: (1) constant temperature on both the top and bottom sides, (2) a circular pattern of temperature variation on the top side with constant temperature on the bottom side, and (3) a circular pattern of temperature variation on both the top and bottom sides. Numerical three-dimensional geometries were constructed as follows: one TEG for the 1-CTEG configuration, two layered TEGs separated by a thermally conductive tape for the 2-CTEG configuration, and three-layered TEGs separated by two thermally conductive tapes for the 3-CTEG configuration. For scenarios (2) and (3), a circular pattern featuring a central circular region surrounded by thick, same-width concentric rings was added to the top side of each configuration for scenario (2) and to both the top and bottom sides for scenario (3). The material properties for alumina ceramics plates, copper interconnectors, and thermally conductive tapes were incorporated into the numerical models. The temperature-dependent thermoelectric properties of Bismuth Telluride for p- and n-type legs were also included in the models. Bismuth Telluride was chosen as the thermoelectric material due to its preferred performance within the temperature range below 250 °C.

The experiments involved three PV-CTEG hybrid systems with InGaP/InGaAs/Ge triple-junction cells (1×1 cm^2, 39.6 % efficiency at 500 suns) on n-CTEGs (TEC1-12710, $n = 1, 2, 3$) layered with thermally conductive tapes. Water-cooled heat sinks were used on the bottom sides of the n-CTEGs. The current (I)- voltage (V) characteristics of the 1-CTEG, 2-CTEG, and 3-CTEG configurations in the PV-1-CTEG, PV-2-CTEG, and PV-3-CTEG hybrid systems were measured at concentrated solar irradiances of 230, 199, and 153 suns, respectively. The irradiance limitation was determined by the triple-junction cells' operating temperature and the cooling capacity of the CTEGs. The short-circuit current (Isc), open-circuit voltage (Voc), and maximum power (Pmax) were used for comparison with simulated results.

Considering the total P_{max} generated by the CTEG configurations, the 1-CTEG configuration generated 0.488 W when the PV-1-CTEG hybrid system was under 230 suns. The 2-CTEG configuration generated 0.718 W when the PV-2-CTEG hybrid system was under 199 suns. The 3-CTEG configuration generated 0.461 W when the PV-3-CTEG hybrid system was under 153 suns.

Comparing the simulated total P_{max} results obtained from the three CTEG configurations under boundary condition scenarios (1)–(3) with the experimental total P_{max} results, it was found that the total P_{max} results for all three configurations aligned more closely with the experimental results under scenario (2). Under scenario (2), the total P_{max} generated by the 1-CTEG configuration, with a circular pattern of temperatures (72, 71, 70, 68, 66, 64, 62, 60, and 58 °C) on the top side and a constant temperature of 19 °C on the bottom side, was 0.483 W, which was 1.0 % lower compared to the experimental total P_{max}. For the 2-CTEG configuration, with a circular pattern of temperatures (109, 108, 107, 105, 103, 101, 99, 97, and 95 °C) on the top side and a constant temperature of 19 °C on the bottom side, the total P_{max} was 0.754 W, 5.0 % higher than the experimental total P_{max}. For the 3-CTEG configuration, with a circular pattern of temperatures (108, 107, 106, 104, 102, 100, 98, 96, and 94 °C) on the top side and a constant temperature of 17 °C on the bottom side, the total P_{max} was 0.508 W, 10.2 % higher than the experimental total P_{max}. This increasing difference between simulated and experimental results can be explained by the fact that the temperature distribution on the hot sides for the TEG2 and TEG3 components was considered uniform, which is a limitation of this simulation. The nonuniform temperature distribution for the hot sides of the TEG2 and TEG3 components will be considered in future work. Scenario (2) yields the best results because, in concentrated light, the intensity of the light falling on the PV-CTEG hybrid systems is nonuniform.

Additionally, the Root Mean Square Error (RMSE) was used as a statistical measure to assess the agreement between simulated and experimental total P_{max} results for the three CTEG configurations (1-CTEG, 2-CTEG, and 3-CTEG) across scenarios (1)–(3). The calculated RMSE values for scenarios (1), (2), and (3) were 0.178, 0.034, and 0.044, respectively. A significant improvement in the RMSE value was observed with the simulated total P_{max} results obtained in scenario (2). Therefore, the alignment between experimental and simulated total P_{max} results was notably accurate for scenario (2).

The close alignment of the simulated total P_{max} results under scenario (2) with experimental results validates the numerical models developed in this study. This validation establishes a reliable method for predicting the performance of CTEG configurations under varying temperature conditions, which is a significant contribution to the field.

Analyzing the three CTEG configurations, it was found that the highest generated total P_{max} was achieved by the 2-CTEG configuration, with a gain of over 47 % compared to the 1-CTEG configuration. The smallest total P_{max} was generated by the 3-CTEG configuration.

The numerical models focused only on the CTEG configurations, excluding concentrated solar irradiance, PV cells, and water-cooled heat sinks. Other temperature patterns, environmental factors (ambient temperature, wind speed, humidity), and aspects like long-term reliability, degradation, and maintenance were not considered. Scaling up to larger systems might introduce complexities not captured in this study. These limitations highlight the need for further research to enhance the understanding and practical application of PV-CTEG hybrid systems.

For future research areas and directions, we suggest exploring novel thermoelectric materials with higher figures of merit (ZT) to enhance the efficiency of CTEG configurations. Conduct optimization studies on the design and configuration of PV-CTEG hybrid systems to maximize efficiency and output power. Use machine learning and artificial intelligence techniques to optimize the operational parameters of hybrid systems.

CRediT authorship contribution statement

Abdelkader Rjafallah: Writing – review & editing, Writing – original draft, Visualization, Software, Methodology, Investigation, Formal analysis, Conceptualization. **Daniel Tudor Cotfas:** Writing – review & editing, Visualization, Validation, Supervision, Project administration, Methodology, Investigation, Formal analysis, Data curation, Conceptualization. **Petru Adrian Cotfas:** Writing – review & editing, Visualization, Validation, Supervision, Project administration, Methodology, Investigation, Formal analysis, Data curation, Conceptualization.

Declaration of competing interest

The authors declare that they have no known competing financial interests or personal relationships that could have appeared to influence the work reported in this paper.

Acknowledgments

The authors express their gratitude to Transilvania University of Brasov for funding this research through the Transilvania Fellowship for Postdoctoral Research/Young Researchers program. We also thank the Synlight facility of the DLR Institute for Future Fuels in Juelich, Germany, for providing access to its installations and for the support of its scientific and technical staff, especially to Dr. Dmitrij Laaber. Additionally, we acknowledge the financial support from the SFERA-III project (Grant Agreement No 823802).

Data availability

Data will be made available on request.

References

[1] S. Mahmoudinezhad, D.T. Cotfas, P.A. Cotfas, E.J.H. Skjølstrup, K. Pedersen, L. Rosendahl, A. Rezania, Experimental investigation on spectrum beam splitting photovoltaic–thermoelectric generator under moderate solar concentrations, Energy 238 (Jan. 2022) 121988.
[2] D.T. Cotfas, P.A. Cotfas, Multiconcept methods to enhance photovoltaic system efficiency, Int. J. Photoenergy 2019 (Nov. 2019) e1905041.
[3] J.-F. Zhong, S.N. Sedeh, Y.-P. Lv, B. Arzani, D. Toghraie, Investigation of Ferro-nanofluid flow within a porous ribbed microchannel heat sink using single-phase and two-phase approaches in the presence of constant magnetic field, Powder Technol. 387 (Jul. 2021) 251–260.
[4] A. Shahsavar, S. Entezari, D. Toghraie, P. Barnoon, Effects of the porous medium and water-silver biological nanofluid on the performance of a newly designed heat sink by using first and second laws of thermodynamics, Chin. J. Chem. Eng. 28 (11) (Nov. 2020) 2928–2937.
[5] H. Arasteh, R. Mashayekhi, M. Goodarzi, S.H. Motaharpour, M. Dahari, D. Toghraie, Heat and fluid flow analysis of metal foam embedded in a double-layered sinusoidal heat sink under local thermal non-equilibrium condition using nanofluid, J. Therm. Anal. Calorim. 138 (2) (Oct. 2019) 1461–1476.
[6] M. Bayat, M.R. Faridzadeh, D. Toghraie, Investigation of finned heat sink performance with nano enhanced phase change material (NePCM), Therm. Sci. Eng. Prog. 5 (Mar. 2018) 50–59.
[7] F. Grubišić Čabo, S. Nižetić, E. Giama, A. Papadopoulos, Techno-economic and environmental evaluation of passive cooled photovoltaic systems in Mediterranean climate conditions, Appl. Therm. Eng. 169 (2020) 114947.
[8] S. Nižetić, I. Marinić-Kragić, F. Grubišić-Čabo, A.M. Papadopoulos, G. Xie, Analysis of novel passive cooling strategies for free-standing silicon photovoltaic panels, J. Therm. Anal. Calorim. 141 (1) (2020) 163–175.
[9] Usman, M.S. Khan, J. Wang, A.A. Memon, T. Muhammad, Investigating the enhanced cooling performance of ternary hybrid nanofluids in a three-dimensional annulus-type photovoltaic thermal system for sustainable energy efficiency, Case Stud. Therm. Eng. 60 (Aug. 2024) 104700.
[10] I. Khan, S. Bilal, T. Salahuddin, A case study on effect of variable viscosity on non-Newtonian nanofluid over an extendable cylindrical surface by utilizing Reynold's model, Alex. Eng. J. 102 (Sep. 2024) 250–263.
[11] N. Zeb Khan, S. Bilal, L. Kolsi, A.S. Shflot, M.Y. Malik, A case study on entropy generation in MHD nanofluid flow in L- shaped triangular corrugated permeable enclosure, Case Stud. Therm. Eng. 59 (Jul. 2024) 104487.
[12] S. Bilal, Asadullah, K. Pan, M. Ramzan, C.A. Saleel, Volumetric thermo-convective and stratified Prandtl fluid magnetized flow over an extended convectively inclined surface with chemically reactive species, Phys. Scripta 99 (2) (Jan. 2024) 025922.
[13] A.A. Memon, Usman, W.A. Khan, T. Muhammad, Numerical investigation of photovoltaic thermal energy efficiency improvement using the backward step containing Cu-Al2O3 hybrid nanofluid, Alex. Eng. J. 75 (Jul. 2023) 391–406.
[14] N. Akkurt, T. Shedd, A.A. Memon, Usman, M.R. Ali, M. Bouye, Analysis of the forced convection via the turbulence transport of the hybrid mixture in three-dimensional L-shaped channel, Case Stud. Therm. Eng. 41 (Jan. 2023) 102558.
[15] Usman, A.A. Memon, H. Anwaar, T. Muhammad, A.A. Alharbi, A.S. Alshomrani, Y.R. Aladwani, A forced convection of water-aluminum oxide nanofluids in a square cavity containing a circular rotating disk of unit speed with high Reynolds number: a Comsol Multiphysics study, Case Stud. Therm. Eng. 39 (Nov. 2022) 102370.
[16] S.S. Joshi, A.S. Dhoble, Photovoltaic -Thermal systems (PVT): technology review and future trends, Renew. Sustain. Energy Rev. 92 (2018) 848–882.
[17] A. Rjafallah, D.T. Cotfas, P.A. Cotfas, Legs geometry influence on the performance of the thermoelectric module, Sustainability 14 (23) (2022) 15823.
[18] M. Benghanem, A.A. Al-Mashraqi, K.O. Daffallah, Performance of solar cells using thermoelectric module in hot sites, Renew. Energy 89 (2016) 51–59.
[19] D. Champier, Thermoelectric generators: a review of applications, Energy Convers. Manag. 140 (2017) 167–181.
[20] Z. Ma, J. Wei, P. Song, M. Zhang, L. Yang, J. Ma, W. Liu, F. Yang, X. Wang, Review of experimental approaches for improving zT of thermoelectric materials, Mater. Sci. Semicond. Process. 121 (2021) 105303.
[21] S. Shittu, G. Li, X. Zhao, X. Ma, Review of thermoelectric geometry and structure optimization for performance enhancement, Appl. Energy 268 (2020) 115075.
[22] Al Khalil, S. Sahnoun, A. Elhassnaoui, S. Yadir, A. Obbadi, Y. Errami, Solar thermoelectric generator and thermoelectric cooler performance: analysis and comparison using a different shape geometry, Clean Energy 7 (6) (Dec. 2023) 1233–1246.
[23] H.C. Luo, L.S. Cheng, Numerical study on optimizing the geometry of segmented asymmetrical thermoelectric generator, IOP Conf. Ser. Earth Environ. Sci. 701 (1) (Mar. 2021) 012022.
[24] Al Khalil, A. Elhassnaoui, S. Yadir, O. Abdellatif, Y. Errami, S. Sahnoun, Performance comparison of TEGs for diverse variable leg geometry with the same leg volume, Energy 224 (Jun. 2021) 119967.
[25] B. Şişik, S. LeBlanc, The influence of leg shape on thermoelectric performance under constant temperature and heat flux boundary conditions, Frontiers in Materials 7 (2020).
[26] H.-B. Liu, S.-L. Wang, Y.-R. Yang, W.-H. Chen, X.-D. Wang, Theoretical analysis of performance of variable cross-section thermoelectric generators: effects of shape factor and thermal boundary conditions, Energy 201 (Jun. 2020) 117660.
[27] Y. Thimont, S. LeBlanc, The impact of thermoelectric leg geometries on thermal resistance and power output, J. Appl. Phys. 126 (9) (Sep. 2019) 095101.
[28] S. Shittu, G. Li, X. Zhao, X. Ma, Y.G. Akhlaghi, E. Ayodele, Optimized high performance thermoelectric generator with combined segmented and asymmetrical

legs under pulsed heat input power, J. Power Sources 428 (Jul. 2019) 53–66.
[29] S. Ferreira-Teixeira, A.M. Pereira, Geometrical optimization of a thermoelectric device: numerical simulations, Energy Convers. Manag. 169 (Aug. 2018) 217–227.
[30] A. Fabián-Mijangos, G. Min, J. Alvarez-Quintana, Enhanced performance thermoelectric module having asymmetrical legs, Energy Convers. Manag. 148 (Sep. 2017) 1372–1381.
[31] S.M. Pourkiaei, M.H. Ahmadi, M. Sadeghzadeh, S. Moosavi, F. Pourfayaz, L. Chen, M.A. Pour Yazdi, R. Kumar, Thermoelectric cooler and thermoelectric generator devices: a review of present and potential applications, modeling and materials, Energy 186 (2019) 115849.
[32] A.Z. Sahin, K.G. Ismaila, B.S. Yilbas, A. Al-Sharafi, A review on the performance of photovoltaic/thermoelectric hybrid generators, Int. J. Energy Res. 44 (5) (2020) 3365–3394.
[33] S. Shittu, G. Li, Y.G. Akhlaghi, X. Ma, X. Zhao, E. Ayodele, Advancements in thermoelectric generators for enhanced hybrid photovoltaic system performance, Renew. Sustain. Energy Rev. 109 (2019) 24–54.
[34] M. Ge, Z. Xuan, G. Zhang, Y. Zhao, Y. Zhao, Effect of non-uniform heat flux on solar thermoelectric generator, Energy Rep. 8 (Dec. 2022) 296–301.
[35] A. Lashin, M. Al Turkestani, M. Sabry, Performance of a thermoelectric generator partially illuminated with highly concentrated light, Energies 13 (14) (Jan. 2020) 3627.
[36] E. Yin, Q. Li, Y. Xuan, Effect of non-uniform illumination on performance of solar thermoelectric generators, Front. Energy 12 (2) (Jun. 2018) 239–248.
[37] T. Ming, Q. Wang, K. Peng, Z. Cai, W. Yang, Y. Wu, T. Gong, The influence of non-uniform high heat flux on thermal stress of thermoelectric power generator, Energies 8 (11) (Nov. 2015) 12584–12602.
[38] B.T. Admasu, X.B. Luo, J.W. Yao, T.Z. Ming, Effects of non-uniform hot junction temperature distribution on the outputs of thermoelectric power generation system, Appl. Mech. Mater. 283 (2013) 87–97.
[39] B.T. Admasu, X. Luo, J. Yao, Effects of temperature non-uniformity over the heat spreader on the outputs of thermoelectric power generation system, Energy Convers. Manag. 76 (Dec. 2013) 533–540.
[40] K. Teffah, Y. Zhang, Modeling and experimental research of hybrid PV-thermoelectric system for high concentrated solar energy conversion, Sol. Energy 157 (Nov. 2017) 10–19.
[41] H.R. Fallah Kohan, F. Lotfipour, M. Eslami, Numerical simulation of a photovoltaic thermoelectric hybrid power generation system, Sol. Energy 174 (Nov. 2018) 537–548.
[42] A. Lashin, M. Al Turkestani, M. Sabry, Concentrated photovoltaic/thermal hybrid system coupled with a thermoelectric generator, Energies 12 (13) (Jan. 2019) 2623.
[43] S. Mahmoudinezhad, A. Rezania, P.A. Cotfas, D.T. Cotfas, L.A. Rosendahl, Transient behavior of concentrated solar oxide thermoelectric generator, Energy 168 (Feb. 2019) 823–832.
[44] M. Sheikholeslami, Z. Khalili, Environmental and energy analysis for photovoltaic-thermoelectric solar unit in existence of nanofluid cooling reporting CO2 emission reduction, J. Taiwan Inst. Chem. Eng. 156 (Mar. 2024) 105341.
[45] M. Sheikholeslami, Z. Khalili, Solar photovoltaic-thermal system with novel design of tube containing eco-friendly nanofluid, Renew. Energy 222 (Feb. 2024) 119862.
[46] M. Sheikholeslami, Z. Khalili, P. Scardi, N. Ataollahi, Concentrated solar photovoltaic cell equipped with thermoelectric layer in presence of nanofluid flow within porous heat sink: impact of dust accumulation, Sustain. Cities Soc. 98 (Nov. 2023) 104866.
[47] M. Sheikholeslami, Z. Khalili, L. Momayez, Efficiency improvement of ternary nanofluid within a solar photovoltaic unit combined with thermoelectric considering environmental analysis, Environ. Technol. Innovat. 32 (Nov. 2023) 103315.
[48] M. Sheikholeslami, Z. Khalili, Investigation of solar Photovoltaic cell utilizing hybrid nanofluid confined jet and helical fins for improving electrical efficiency in existence of thermoelectric module, Appl. Therm. Eng. 234 (Nov. 2023) 121329.
[49] M. Sheikholeslami, Z. Khalili, Investigation of solar photovoltaic-thermoelectric system for building unit in presence of helical tapes and jet impingement of hybrid nanomaterial, J. Build. Eng. 74 (Sep. 2023) 106871.
[50] V.S. Poddar, V.A. Ranawade, N.B. Dhokey, Study of synergy between photovoltaic, thermoelectric and direct evaporative cooling system for improved performance, Renew. Energy 182 (Jan. 2022) 817–826.
[51] A. Rjafallah, A. Younis, D.T. Cotfas, P.A. Cotfas, Effects of temperature uniformity and nonuniformity on thermoelectric generator performance across hot and cold sides, Case Stud. Therm. Eng. 59 (Jul. 2024) 104596.
[52] COMSOL Multiphysics." [Online]. Available: https://www.comsol.com..
[53] AG TermoPasty." [Online]. Available: https://termopasty.com..
[54] S. Shittu, G. Li, Q. Xuan, X. Xiao, X. Zhao, X. Ma, Y.G. Akhlaghi, Transient and non-uniform heat flux effect on solar thermoelectric generator with phase change material, Appl. Therm. Eng. 173 (Jun. 2020) 115206.
[55] A. Prasad, R.C. Thiagarajan, Multiphysics modelling and multilevel optimization of thermoelectric generator for waste heat recovery, in: Presented at the COMSOL Conference 2018 Bangalore, ITC Gardenia, 2018.
[56] D.T. Cotfas, P.A. Cotfas, O.M. Machidon, Study of temperature coefficients for parameters of photovoltaic cells, Int. J. Photoenergy 2018 (1) (2018) 5945602.
[57] K. Tyagi, B. Gahtori, S. Kumar, S.R. Dhakate, Advances in solar thermoelectric and photovoltaic-thermoelectric hybrid systems for power generation, Sol. Energy 254 (Apr. 2023) 195–212.
[58] B. Yang, S. Wu, J. Huang, Z. Guo, J. Wang, Z. Zhang, R. Xie, H. Shu, L. Jiang, Salp swarm optimization algorithm based MPPT design for PV-TEG hybrid system under partial shading conditions, Energy Convers. Manag. 292 (Sep. 2023) 117410.